A fast iterative scheme for the linearized Boltzmann equation

Journal of Computational Physics 338 (2017) 431–451

Contents lists available at ScienceDirect

Journal of Computational Physics

www.elsevier.com/locate/jcp

A fast iterative scheme for the linearized Boltzmann equation

Lei Wu [a,*], Jun Zhang [c], Haihu Liu [d], Yonghao Zhang [a], Jason M. Reese [b]

[a] James Weir Fluids Laboratory, Department of Mechanical and Aerospace Engineering, University of Strathclyde, Glasgow G1 1XJ, UK
[b] School of Engineering, University of Edinburgh, Edinburgh EH9 3FB, UK
[c] School of Aeronautic Science and Engineering, Beihang University, Beijing 100191, China
[d] School of Energy and Power Engineering, Xi'an Jiaotong University, 28 West Xianning Road, Xi'an 710049, China

ARTICLE INFO

Article history:
Received 22 June 2016
Received in revised form 1 March 2017
Accepted 2 March 2017
Available online 7 March 2017

Keywords:
Linearized Boltzmann equation
Rarefied gas dynamics
Synthetic iterative scheme
Lennard–Jones potential
Gas mixture

ABSTRACT

Iterative schemes to find steady-state solutions to the Boltzmann equation are efficient for highly rarefied gas flows, but can be very slow to converge in the near-continuum flow regime. In this paper, a synthetic iterative scheme is developed to speed up the solution of the linearized Boltzmann equation by penalizing the collision operator L into the form $L = (L + N\delta h) - N\delta h$, where δ is the gas rarefaction parameter, h is the velocity distribution function, and N is a tuning parameter controlling the convergence rate. The velocity distribution function is first solved by the conventional iterative scheme, then it is corrected such that the macroscopic flow velocity is governed by a diffusion-type equation that is asymptotic-preserving into the Navier–Stokes limit. The efficiency of this new scheme is assessed by calculating the eigenvalue of the iteration, as well as solving for Poiseuille and thermal transpiration flows. We find that the fastest convergence of our synthetic scheme for the linearized Boltzmann equation is achieved when $N\delta$ is close to the average collision frequency. The synthetic iterative scheme is significantly faster than the conventional iterative scheme in both the transition and the near-continuum gas flow regimes. Moreover, due to its asymptotic-preserving properties, the synthetic iterative scheme does not need high spatial resolution in the near-continuum flow regime, which makes it even faster than the conventional iterative scheme. Using this synthetic scheme, with the fast spectral approximation of the linearized Boltzmann collision operator, Poiseuille and thermal transpiration flows between two parallel plates, through channels of circular/rectangular cross sections and various porous media are calculated over the whole range of gas rarefaction. Finally, the flow of a Ne–Ar gas mixture is solved based on the linearized Boltzmann equation with the Lennard–Jones intermolecular potential for the first time, and the difference between these results and those using the hard-sphere potential is discussed.

1. Introduction

The Boltzmann equation is fundamental to a broad range of applications from aerodynamics to microfluidics [1], and it is important to be able to solve it accurately and efficiently. Most often, the Boltzmann equation is solved by the stochastic Direct Simulation Monte Carlo (DSMC) technique, which uses a number of simulated particles to mimic the binary collisions

* Corresponding author.
E-mail address: lei.wu.100@strath.ac.uk (L. Wu).

http://dx.doi.org/10.1016/j.jcp.2017.03.002
0021-9991/

and streaming of very large numbers of gas molecules [2]. In DSMC, the length of the spatial cell and the time step need to be smaller than the local molecular mean free path and the mean collision time, respectively, and for this reason the technique becomes very slow and costly for near-continuum flows. Although time-relaxed and asymptotic-preserving Monte Carlo methods allow larger time steps [3,4], the restriction on the size of the spatial cells has not yet been removed. The same problem, in fact, exists in deterministic numerical methods for the Boltzmann equation, where the streaming and the collisions are treated separately in the splitting scheme [5,6].

The unified gas-kinetic scheme (UGKS) provides an alternative approach. It was first developed for the Bhatnagar–Gross–Krook (BGK) kinetic model [7,8], then for the Shakhov model [9,10], and finally generalized to the Boltzmann equation [11]. It handles the streaming and binary collisions simultaneously so that, for time-dependent problems, the time step is only limited by the Courant–Friedrichs–Lewy condition. Also, the UGKS is asymptotic-preserving into the Navier–Stokes limit [12], so the length of the spatial cells can be significantly larger than the molecular mean free path. Moreover, the UGKS is a finite volume method, and the analytical integral solution of the BGK-type model enables accurate flux evaluation at the cell interface, so that the essential flow physics can be captured even with the coarse grids. These advanced properties make the UGKS (and its improved version: the discrete UGKS [13,14]) a multiscale method for efficient and accurate calculations of rarefied gas flows over a wide range of the gas rarefaction. Recently, an implicit UGKS has been proposed to eliminate the time step limitation and further improve the numerical efficiency [15].

To find a steady-state solution to the Boltzmann equation, an iterative scheme is often used. In the free-molecular flow regime, where binary collisions are negligible, an iterative scheme is efficient, because the gas molecules move in straight way (except the collision with wall surfaces) so that any disturbance at one point can be quickly felt by all other points. However, for near-continuum flows the iterations converge slowly and the results are very likely to be biased by accumulated rounding errors. Although the time and spatial steps can be large, the UGKS still needs a large number of iterations [15]. This is governed by the underlying physics: the exchange of information through streaming becomes very inefficient when binary collisions dominate. Therefore, it would be useful to develop an efficient numerical scheme to solve the Boltzmann equation that both has the asymptotic-preserving property in the Navier–Stokes limit (like the UGKS where the spatial resolution can be coarse) and converges to the steady-state rapidly.

Inspired by work on fast iterative methods for radiation transport processes [16], accelerated iterative schemes have been developed for the linearized BGK and Shahkov models [17] to overcome slow convergence in the near-continuum flow regime. The fast iterative scheme is called a "synthetic iterative scheme" (SIS) since kinetic model equations are solved in parallel with diffusion-type equations for macroscopic quantities such as the flow velocity and heat flux. The SIS has been successfully applied to Poiseuille flow in channels with two-dimensional cross sections of arbitrary shapes [18] using a BGK model for single-species gases, and flows of binary and ternary gas mixtures driven by local pressure, temperature, and concentration gradients [19–21,18,22–24] using the McCormack model [25]. The fast convergence of the SIS is due to three factors: first, the macroscopic synthetic diffusion-type equations exchange the information very efficiently; second, the macroscopic flow quantities can be fed back into mesoscopic kinetic models; and third, macroscopic diffusion-type equations are solved more quickly than mesoscopic kinetic model equations.

In the present paper we develop a SIS to solve the linearized Boltzmann equation (LBE) for Poiseuille and thermal transpiration flows. Although for the single-species LBE these canonical flows have been extensively studied for hard-sphere [26,27], inverse power-law [28], and even Lennard–Jones [29,30] potentials, numerical results for near-continuum flows are scarce. Moreover, for gas mixtures these flows have only been solved based on the hard-sphere model in a one-dimensional geometry [31]. We will calculate these flows through two-dimensional cross sections of arbitrary shape, and investigate the influence of realistic intermolecular potentials for gas mixtures. The core methods we adopt are (i) the SIS originally developed for kinetic model equations, which is introduced in the previous paragraph, (ii) the penalization method [6,32,33], which makes the development of SIS for the LBE possible, and (iii) the fast spectral method, developed by Mouhot and Pareschi [34] and extended by us to gas mixtures and Lennard–Jones potentials [35,30], which enables the efficient and accurate computation of the linearized Boltzmann collision operator.

The rest of this paper is organized as follows. In Sec. 2, we briefly introduce the LBE for single-species gases and the conventional iterative scheme (CIS). Then, by analyzing the SIS for the BGK model, we develop a SIS for the LBE and test its performance by calculating both the eigenvalues of iterations and Poiseuille/thermal transpiration flows. We improve the efficiency of the proposed SIS by adjusting a parameter in the scheme, which can be determined prior to the numerical simulation. In Sec. 3, the SIS is used to solve rarefied gas flows in multiscale problems. In Sec. 4, the SIS in polar coordinates is proposed and numerical results of the LBE for Poiseuille flow through a tube are presented. In Sec. 5, the SIS is extended to the LBE for gas mixtures, and Poiseuille flow of a Ne–Ar mixture is solved for the first time based on the Lennard–Jones potential. In Sec. 6, we conclude with a summary of the new numerical method and future perspectives.

2. A synthetic scheme for the single-species LBE

Consider the steady flow of a single-species monatomic gas along a channel of arbitrary cross section in the x_1–x_2 plane, subject to small pressure/temperature gradients in the x_3 direction. The velocity distribution function (VDF) can be expressed as $f = f_{eq} + h$, where

$$f_{eq}(\mathbf{v}) = \frac{\exp(-|\mathbf{v}|^2)}{\pi^{3/2}} \tag{1}$$

is the equilibrium VDF and $h(x_1, x_2, \mathbf{v})$ is the perturbed VDF satisfying $|h/f_{eq}| \ll 1$. The LBE for h is:

$$v_1 \frac{\partial h}{\partial x_1} + v_2 \frac{\partial h}{\partial x_2} = L(h, f_{eq}) + S, \tag{2}$$

with the linearized Boltzmann collision operator [28]:

$$L = \underbrace{\iint B(|\mathbf{v} - \mathbf{v}_*|, \theta)[f_{eq}(\mathbf{v}')h(\mathbf{v}'_*) + f_{eq}(\mathbf{v}'_*)h(\mathbf{v}') - f_{eq}(\mathbf{v})h(\mathbf{v}_*)]d\Omega d\mathbf{v}_*}_{L^+} - \nu_{eq}(\mathbf{v})h(\mathbf{v}). \tag{3}$$

From Eq. (1) to (3), $\mathbf{x} = (x_1, x_2, x_3)$ is the position vector normalized by the characteristic flow length ℓ, $\mathbf{v} = (v_1, v_2, v_3)$ is the molecular velocity vector normalized by the most probable speed $v_m = \sqrt{2k_B T_0/m}$ (k_B is the Boltzmann constant, T_0 is the gas/wall temperature, and m is the gas molecular mass), $B(|\mathbf{v} - \mathbf{v}_*|, \theta)$ is the collision kernel determined by the intermolecular potential [28,30], and

$$\nu_{eq}(\mathbf{v}) = \iint B(|\mathbf{v} - \mathbf{v}_*|, \theta) f_{eq}(\mathbf{v}_*) d\Omega d\mathbf{v}_* \tag{4}$$

is the equilibrium collision frequency.

Finally, S is the source term:

$$S = \begin{cases} -X_P v_3 f_{eq}, & \text{for Poiseuille flow,} \\ -X_T v_3 (|\mathbf{v}|^2 - 5/2) f_{eq}, & \text{for thermal transpiration flow,} \end{cases} \tag{5}$$

where X_P and X_T are the pressure and temperature gradients, respectively. For the LBE, since macroscopic quantities are proportional to X_P and X_T, we assume $X_P = X_T = -1$.

The macroscopic quantities of interest are the flow velocity normalized by the most probable speed:

$$U_3 = \int v_3 h d\mathbf{v}, \tag{6}$$

the shear stresses normalized by the equilibrium gas pressure p_0:

$$P_{13} = \int 2 v_1 v_3 h d\mathbf{v}, \quad P_{23} = \int 2 v_2 v_3 h d\mathbf{v}, \tag{7}$$

and the heat flux normalized by $p_0 v_m$:

$$q_3 = \int \left(|\mathbf{v}|^2 - 5/2\right) v_3 h d\mathbf{v}. \tag{8}$$

The dimensionless mass flow rate M and heat flow rate Q are:

$$\begin{aligned} \mathcal{M} &= \frac{1}{A} \iint U_3 dx_1 dx_2, \\ \mathcal{Q} &= \frac{1}{A} \iint q_3 dx_1 dx_2, \end{aligned} \tag{9}$$

where A is the area of the cross section.

The integro-differential system defined by Eqs. (2) and (3) is usually solved by the CIS. Given the value of $h^{(k)}$ at the k-th iteration step, the VDF at the next iteration step is calculated by solving the following equation:

$$\nu_{eq} h^{(k+1)} + v_1 \frac{\partial h^{(k+1)}}{\partial x_1} + v_2 \frac{\partial h^{(k+1)}}{\partial x_2} = L^+(h^{(k)}, f_{eq}) + S, \tag{10}$$

where derivatives with respect to spatial variables are usually approximated by a second-order upwind finite difference. The process is repeated until relative differences between successive estimates of macroscopic quantities are less than a convergence criterion ϵ. The number of iteration steps in CIS increases significantly when the ratio of the molecular mean free path to the characteristic flow length decreases, especially when the gas flow is in the near-continuum regime [17], see also the data in Table 1 below. It is our goal here to develop a fast iterative scheme to solve the LBE efficiently and accurately over the whole range of gas rarefaction.

2.1. SIS for the BGK equation

To begin with, we introduce the SIS for the BGK equation [17]. The linearized Boltzmann collision operator in Eq. (3) is replaced by that of the BGK kinetic model, yielding the following equation for the perturbed VDF h:

$$v_1\frac{\partial h}{\partial x_1}+v_2\frac{\partial h}{\partial x_2}=\underbrace{\delta[2U_3v_3f_{eq}-h]}_{L_{BGK}}+S, \tag{11}$$

where

$$\delta=\frac{p_0\ell}{\mu v_m} \tag{12}$$

is the rarefaction parameter, with μ being the gas shear viscosity.

Multiplying Eq. (11) by the Hermite polynomials and applying the recursion relation, a set of first-order partial differential equations can be obtained for various orders of moments [36]. Here, two relevant equations for the macroscopic flow velocity are listed:

$$\frac{\partial U_3}{\partial x_1}=-\delta P_{13}-\frac{1}{4}\frac{\partial F_{2,0,1}}{\partial x_1}-\frac{1}{4}\frac{\partial F_{1,1,1}}{\partial x_2}, \tag{13}$$

$$\frac{\partial U_3}{\partial x_2}=-\delta P_{23}-\frac{1}{4}\frac{\partial F_{1,1,1}}{\partial x_1}-\frac{1}{4}\frac{\partial F_{0,2,1}}{\partial x_2}, \tag{14}$$

where

$$F_{m,n,l}(x_1,x_2)=\int h(x_1,x_2,\mathbf{v})H_m(v_1)H_n(v_2)H_l(v_3)d\mathbf{v} \tag{15}$$

are the non-accelerated high-order moments, with $H_n(v)$ being the n-th order physicists' Hermite polynomial. The combination of Eqs. (13) and (14) leads to an equation of diffusion-type for the flow velocity:

$$\frac{\partial^2U_3}{\partial x_1^2}+\frac{\partial^2U_3}{\partial x_2^2}=-\delta\left(\frac{\partial P_{13}}{\partial x_1}+\frac{\partial P_{23}}{\partial x_2}\right)-\frac{1}{4}\left(\frac{\partial^2F_{2,0,1}}{\partial x_1^2}+2\frac{\partial^2F_{1,1,1}}{\partial x_1\partial x_2}+\frac{\partial^2F_{0,2,1}}{\partial x_2^2}\right) \tag{16a}$$

$$=\begin{cases}-\delta-\frac{1}{4}\left(\frac{\partial^2F_{2,0,1}}{\partial x_1^2}+2\frac{\partial^2F_{1,1,1}}{\partial x_1\partial x_2}+\frac{\partial^2F_{0,2,1}}{\partial x_2^2}\right), & \text{Poiseuille},\\ -\frac{1}{4}\left(\frac{\partial^2F_{2,0,1}}{\partial x_1^2}+2\frac{\partial^2F_{1,1,1}}{\partial x_1\partial x_2}+\frac{\partial^2F_{0,2,1}}{\partial x_2^2}\right), & \text{thermal transpiration}.\end{cases} \tag{16b}$$

Note that in obtaining the final equation we have used the relation $\partial P_{13}/\partial x_1+\partial P_{23}/\partial x_2=1$ for Poiseuille flow and $\partial P_{13}/\partial x_1+\partial P_{23}/\partial x_2=0$ for thermal transpiration flow. The SIS for the BGK equation then works as follows [17,36]:

- When $h^{(k)}$ and $U_3^{(k)}$ are known at the k-th iteration step, calculate the VDF $h^{(k+1)}$ by solving the following equation:

$$\delta h^{(k+1)}+v_1\frac{\partial h^{(k+1)}}{\partial x_1}+v_2\frac{\partial h^{(k+1)}}{\partial x_2}=2\delta U_3^{(k)}v_3f_{eq}+S. \tag{17}$$

- From $h^{(k+1)}$, calculate the non-accelerated moments $F_{2,0,1}$, $F_{1,1,1}$, and $F_{0,2,1}$.
- From $h^{(k+1)}$, calculate the flow velocity $U_3^{(k+1)}$ near the boundary. However, for the flow velocity in the bulk (i.e. several computational layers away from the boundary), $U_3^{(k+1)}$ is obtained by solving the diffusion-type equation (16b).

The above iterative procedure is continued until convergence. It should be emphasized that the relation $\partial P_{13}/\partial x_1+\partial P_{23}/\partial x_2=1$ or 0 for Poiseuille flow or thermal transpiration flow, respectively, is crucial for the fast convergence of the SIS. This is because non-accelerated moments are negligible at large values of the rarefaction parameter δ, so the synthetic equation (16b) quickly adjusts the flow velocity to the solution of the Navier–Stokes equation,

$$\begin{aligned}&\frac{\partial^2U_3}{\partial x_1^2}+\frac{\partial^2U_3}{\partial x_2^2}=-\delta, \quad \text{for Poiseuille flow},\\ &\frac{\partial^2U_3}{\partial x_1^2}+\frac{\partial^2U_3}{\partial x_2^2}=0, \quad \text{for thermal transpiration flow},\end{aligned} \tag{18}$$

which is close to the solution of the linearized BGK equation. If the synthetic equation (16a) is used instead, with P_{13} and P_{23} calculated based on the VDF obtained at each iteration step, the slow convergence at large values of δ is not

improved because it takes a lot of iterations to reach the condition $\partial P_{13}/\partial x_1 + \partial P_{23}/\partial x_2 = 1$ or 0; in the worst-case scenario, it may even lead to false convergence and incorrect solutions when the spatial resolution is not high enough. However, Eq. (16b) guarantees the correctness of the solution at large values of δ, as it has the asymptotic-preserving property in the Navier–Stokes limit [12]. This point will be demonstrated in Sec. 2.6 below.

2.2. SIS for the LBE

The development of a SIS for the LBE is not straightforward, since the collision operator of the LBE is much more complicated than that of the linearized BGK model. Directly following the method in Sec. 2.1, the following diffusion-type equation for the flow velocity is obtained:

$$\frac{\partial^2 U_3}{\partial x_1^2} + \frac{\partial^2 U_3}{\partial x_2^2} = 2\frac{\partial}{\partial x_1}\int v_1 v_3 L d\mathbf{v} + 2\frac{\partial}{\partial x_2}\int v_2 v_3 L d\mathbf{v} - \frac{1}{4}\left(\frac{\partial^2 F_{2,0,1}}{\partial x_1^2} + 2\frac{\partial^2 F_{1,1,1}}{\partial x_1 \partial x_2} + \frac{\partial^2 F_{0,2,1}}{\partial x_2^2}\right), \tag{19}$$

which, like Eq. (16a), cannot improve the slow convergence at large values of δ.

To speed up the convergence, the relation $\partial P_{13}/\partial x_1 + \partial P_{23}/\partial x_2 = 1$ or 0 for Poiseuille flow or thermal transpiration flow, respectively, must be reflected in the diffusion-type equation. For instance, as in Eq. (16b), a term similar to $-\delta$ should appear on the right-hand-side of Eq. (19) for Poiseuille flow. To achieve this, we penalize the linearized Boltzmann collision operator by the linearized BGK operator [6], i.e.,

$$L = (L - L_{BGK}) + L_{BGK}, \tag{20}$$

and let

$$\begin{aligned} 2\int v_1 v_3 L d\mathbf{v} &= 2\int v_1 v_3 (L - L_{BGK}) d\mathbf{v} - \delta P_{13}, \\ 2\int v_2 v_3 L d\mathbf{v} &= 2\int v_2 v_3 (L - L_{BGK}) d\mathbf{v} - \delta P_{23}. \end{aligned} \tag{21}$$

This transforms Eq. (19) into

$$\begin{aligned} \frac{\partial^2 U_3}{\partial x_1^2} + \frac{\partial^2 U_3}{\partial x_2^2} = &-\delta - \frac{1}{4}\left(\frac{\partial^2 F_{2,0,1}}{\partial x_1^2} + 2\frac{\partial^2 F_{1,1,1}}{\partial x_1 \partial x_2} + \frac{\partial^2 F_{0,2,1}}{\partial x_2^2}\right) \\ &+ 2\frac{\partial}{\partial x_1}\int v_1 v_3 (L - L_{BGK}) d\mathbf{v} + 2\frac{\partial}{\partial x_2}\int v_2 v_3 (L - L_{BGK}) d\mathbf{v}, \end{aligned} \tag{22}$$

which is very close to Eq. (16b) for the linearized BGK equation. At large values of the rarefaction parameter δ, $\int (L - L_{BGK}) v_1 v_3 d\mathbf{v}$ and $\int (L - L_{BGK}) v_2 v_3 d\mathbf{v}$ approach zero, and Eq. (22) possesses the asymptotic-preserving property in the Navier–Stokes limit [12]. Therefore, a SIS can be developed based on this equation. Note that for thermal transpiration flow, δ in Eq. (22) should be replaced by zero, as $\partial P_{13}/\partial x_1 + \partial P_{23}/\partial x_2 = 0$.

The SIS for the LBE then works as that for the BGK equations, with some changes:

- When $h^{(k)}$ and $U_3^{(k)}$ are known at the k-th iteration step, we calculate $\int v_1 v_3 (L - L_{BGK}) d\mathbf{v}$ and $\int v_2 v_3 (L - L_{BGK}) d\mathbf{v}$. We also calculate the VDF $h^{(k+1/2)}$ by solving the following equation:

$$v_{eq} h^{(k+1/2)} + v_1 \frac{\partial h^{(k+1/2)}}{\partial x_1} + v_2 \frac{\partial h^{(k+1/2)}}{\partial x_2} = L^+(h^{(k)}, f_{eq}) + S. \tag{23}$$

- From $h^{(k+1/2)}$, we calculate the flow velocity $U^{(k+1/2)}$, and the non-accelerated moments $F_{2,0,1}$, $F_{1,1,1}$, and $F_{0,2,1}$.
- Near the boundary, we let $U_3^{(k+1)} = U_3^{(k+1/2)}$, while we solve the diffusion-type equation (22) to obtain the flow velocity in the bulk.
- A correction of the VDF is introduced in accordance with the changed flow velocity:

$$h^{(k+1)} = h^{(k+1/2)} + 2(U_3^{(k+1)} - U_3^{(k+1/2)}) v_3 f_{eq}. \tag{24}$$

- The above steps are repeated until convergence.

Note that for the linearized BGK model [17], Eq. (24) is not necessary because the linearized collision operator at the next iterative step automatically changes when the flow velocity is corrected by the diffusion-type equation. In the LBE, however, the change of flow velocity does not directly change the collision operator at the next iterative step, so Eq. (24) is important.

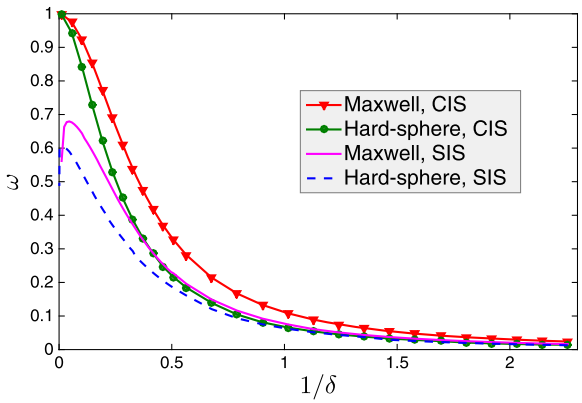

Fig. 1. Eigenvalue ω versus the inverse rarefaction parameter $1/\delta$ for different iterative schemes for the LBE with Maxwell and hard-sphere molecules (Note that Poiseuille and thermal transpiration flows have the same eigenvalue). Our method to calculate the eigenvalue for the SIS at large values of δ is not accurate, since the convergence is so fast (it converges after one iteration) that we have few data to calculate λ through numerical fitting. However, the trend that ω in the SIS decreases with $1/\delta$ is clear when $1/\delta \to 0$.

2.3. Numerical analysis of the convergence rate

Analytical solutions for the eigenvalue ω have previously been introduced in order to characterize the convergence rate of the iterative scheme for the linearized BGK equation [17,36]. However, this is more difficult for the LBE because of its intricate collision operator. Here we calculate the eigenvalue numerically in order to study the performance of both the SIS and the CIS. For simplicity, we consider a periodic system of length ℓ in the x_1 direction, while the system is homogeneous in the x_2 direction.

For the CIS described by Eq. (10), the VDF is solved in the following manner (hereafter in this section, h and U_3 should be viewed as their Fourier transforms in the x_1 direction):

$$h^{(k+1)} = \frac{L^+(h^{(k)}, f_{eq}) + S}{\nu_{eq} + 2i\pi v_1}, \quad i = \sqrt{-1}. \tag{25}$$

During iteration, the flow velocity $U_3^{(k+1)} = \int h^{(k+1)} v_3 d\mathbf{v}$ is recorded, and upon convergence the resultant series of the flow velocity is fitted by $U_3(k) = U_{3\infty} + Ce^{-\lambda k}$. The eigenvalue ω is then calculated as $\omega = e^{-\lambda}$. It is obvious that the smaller ω is, the faster the convergence; the case of $\omega = 1$ means no convergence.

For the SIS, the VDF is first updated according to Eq. (23):

$$h^{(k+1/2)} = \frac{L^+(h^{(k)}, f_{eq}) + S}{\nu_{eq} + 2i\pi v_1}. \tag{26}$$

Then the flow velocity is calculated according to the diffusion-type equation (22) as

$$U_3^{(k+1)} = \begin{cases} (\delta - 2i\pi A_1 - 4\pi^2 A_2)/4\pi^2, & \text{Poiseuille,} \\ (-2i\pi A_1 - 4\pi^2 A_2)/4\pi^2, & \text{thermal transpiration,} \end{cases} \tag{27}$$

where $A_1 = 2\int v_1 v_3 (L - L_{BGK})|_{h=h^{(k)}} d\mathbf{v}$ and $A_2 = \int h^{(k+1/2)}(2v_1^2 - 1) v_3 d\mathbf{v}$. Finally, this flow velocity is used to correct the VDF according to Eq. (24): $h^{(k+1)} = h^{(k+1/2)} + 2(U_3^{(k+1)} - U_3^{(k+1/2)}) v_3 f_{eq}$, where $U_3^{(k+1/2)} = \int h^{(k+1/2)} v_3 d\mathbf{v}$. The calculation of the eigenvalue for the SIS then follows in the same way as that for the CIS.

Figure 1 presents the eigenvalues for both the SIS and the CIS. For small values of the rarefaction parameter δ both schemes have the same convergence rate. However, for large values of δ, the CIS has extremely slow convergence ($\omega \approx 1$), while the SIS converges much faster. It is also interesting to note that the intermolecular potential greatly affects the convergence rate: at the same value of δ, the solution of the LBE for hard-sphere molecules converges faster than that for Maxwell molecules,[1] in both the SIS and the CIS.

2.4. Numerical results for spatially-inhomogeneous systems

We now present numerical simulations that demonstrate the efficiency and accuracy of the SIS for Poiseuille/thermal transpiration flows between infinite parallel plates and through a two-dimensional square channel.

[1] We assume the collision kernel $B(|\mathbf{v} - \mathbf{v}_*|, \theta)$ for Maxwell molecules is proportional to $1/\sqrt{\sin\theta}$, where θ is the deflection angle during binary collisions, see Eq. (2.3) in Ref. [28].

Table 1
Mass/heat flow rates in the Poiseuille flow of hard-sphere and Maxwell molecules between two parallel plates. Itr denotes the number of iteration steps to reach the convergence criterion $\epsilon = 10^{-10}$. The results for the CIS are not shown at $\delta = 100$ because it is hard to converge.

δ	Hard-sphere molecules						Maxwell molecules					
	SIS			CIS			SIS			CIS		
	Itr	$\mathcal{M}$	$-\mathcal{Q}$	Itr	$\mathcal{M}$	$-\mathcal{Q}$	Itr	$\mathcal{M}$	$-\mathcal{Q}$	Itr	$\mathcal{M}$	$-\mathcal{Q}$
0.01	9	1.454	0.658	9	1.454	0.658	10	1.352	0.549	10	1.352	0.549
0.05	12	1.098	0.470	12	1.098	0.470	16	1.033	0.398	16	1.033	0.398
0.1	15	0.974	0.398	15	0.974	0.398	20	0.926	0.344	20	0.926	0.344
0.5	32	0.781	0.252	33	0.781	0.252	46	0.767	0.233	48	0.767	0.233
1	40	0.754	0.195	49	0.754	0.195	59	0.751	0.188	71	0.751	0.188
2	49	0.782	0.141	91	0.782	0.141	66	0.789	0.143	137	0.789	0.143
5	54	0.977	0.079	283	0.977	0.079	71	0.992	0.085	431	0.992	0.085
10	54	1.365	0.045	777	1.364	0.045	72	1.383	0.050	1183	1.382	0.050
20	55	2.182	0.024	2432	2.177	0.024	72	2.199	0.027	3684	2.194	0.027
30	54	3.009	0.016	4798	3.000	0.016	71	3.025	0.019	7245	3.017	0.019
50	54	4.671	0.010	12038	4.649	0.010	72	4.686	0.012	18136	4.665	0.012
100	55	8.836	0.005				73	8.848	0.006			

We first consider a gas flow between two infinite parallel plates located at $x_1 = -1/2$ and $x_1 = 1/2$ (note that x_1 has been normalized by the distance between two parallel palates ℓ). Pressure and temperature gradients are applied in the x_3 direction only, so the flow is homogeneous in the x_2 direction and partial derivatives with respect to x_2 can be dropped. The discretization of the three-dimensional molecular velocity space, as well as the fast spectral method to solve the linearized Boltzmann collision operator, are given in Ref. [28]. We adopt the diffuse boundary condition for the gas–wall interaction. Due to symmetry, only half of the spatial region ($-1/2 \le x_1 \le 0$) is simulated, with a specular-reflection boundary condition at $x_1 = 0$, and the diffuse boundary condition $h(v_2 > 0) = 0$ at $x_1 = -1/2$. The spatial domain is divided into 100 nonuniform sections, with most of the discrete points placed near the wall: $x_1 = (10 - 15s + 6s^2)s^3 - 0.5$, where $s = (0, 1, \cdots, N_s)/2N_s$. The size of the smallest section is 1.24×10^{-6}, small enough to capture the Knudsen layer.

For the one-dimensional problem, the shear stress is $P_{13} = x_1$ for Poiseuille flow and $P_{13} = 0$ for thermal transpiration flow. The diffusion-type equation (22) is integrated to give the following first-order ordinary differential equation:

$$\frac{\partial U_3}{\partial x_1} = -\delta P_{13} - \frac{1}{4}\frac{\partial F_{2,0,1}}{\partial x_1} + 2\int v_1 v_3 (L - L_{BGK}) d\mathbf{v}, \tag{28}$$

which is solved by a second-order upwind finite difference (with a first-order scheme at the wall), with the boundary condition $U_3(x_1 = -1/2) = \int v_3 h(x_1 = -1/2) d\mathbf{v}$ calculated from the VDF at each iteration. The iterations terminate when the relative errors in the mass and heat flow rates ($\mathcal{M} = 2\int_{-1/2}^{0} U_3 dx_1$, $\mathcal{Q} = 2\int_{-1/2}^{0} q_3 dx_1$) between two consecutive iterations are less than $\epsilon = 10^{-10}$.

A comparison between the SIS and the CIS is tabulated in Table 1 for Poiseuille flow. The relative differences in mass/heat flow rates between the two schemes is less than 0.5%, which demonstrates the accuracy of the SIS. The superiority of the SIS over the CIS is immediately seen: for the CIS, the number of iteration steps increases rapidly with the rarefaction parameter, while for the SIS it only slightly increases with δ in the free-molecular and transition flow regimes and saturates in the near-continuum flow regime ($\delta \ge 10$). Since, compared to the fast spectral approximation to the Boltzmann collision operator the time for solving Eq. (28) is negligible, the CPU time saving is proportional to the time-step saving, and this is tremendous for the SIS. At $\delta = 10$, the SIS is about 15 times faster than the CIS, while at $\delta = 50$ it is about 220 times faster.

It is interesting to note that for both the SIS and CIS, solutions of the LBE for hard-sphere molecules converge about 1.5 times faster than for Maxwell molecules, a result which supports the convergence analysis in Sec. 2.3.

We also consider Poiseuille/thermal transpiration flows along a channel of square cross section. Due to symmetry, only one quarter of the spatial domain is simulated, which is divided into 50×50 non-uniform cells: in each direction, from the boundary to the center, the length of each cell side forms a geometric progression with a common ratio 1.05. The diffusion-type equation (22) is discretized by a five-point central difference, and solved by the successive-over-relaxation method [37]. Table 2 summarizes the numerical results from the SIS. The mass flow rate in thermal transpiration flow is not shown, as according to the Onsager–Casimir relation it is equal to the heat flow rate in Poiseuille flow. From this table it is seen that our SIS for the LBE works efficiently over the whole range of gas rarefaction.

This efficient SIS can also be used to calculate the slip coefficients. In Ref. [38] it was stated in that the thermal slip coefficient is strongly affected by the intermolecular potential. Therefore, we calculate this coefficient based on the LBE for hard-sphere and Maxwellian molecules, and compare our results to that of the Shakhov kinetic model [39]. Since in the near-continuum regime, the dimensionless mass flow rate in a thermal transpiration flow can be expressed as [40]

$$\mathcal{M}_T = \frac{2\sigma_T}{\delta}, \tag{29}$$

we calculate the thermal slip coefficient as $\sigma_T = 2\delta\mathcal{M}_T$ by choosing large values of δ.

Table 2
Mass/heat flow rates in Poiseuille/thermal transpiration flows of hard-sphere and Maxwell molecules along a channel of square cross section, as well as the number of iterations (Itr) to reach the convergence criterion $\epsilon = 10^{-10}$ in the SIS.

δ	Hard-sphere molecules					Maxwell molecules				
	Itr	$\mathcal{M}_P$	$-\mathcal{Q}_P$	Itr	$\mathcal{Q}_T$	Itr	$\mathcal{M}_P$	$-\mathcal{Q}_P$	Itr	$\mathcal{Q}_T$
0.0	3	0.419	0.210	3	0.944	3	0.419	0.210	3	0.944
0.01	5	0.413	0.205	5	0.924	6	0.411	0.201	5	0.918
0.05	6	0.402	0.194	6	0.882	7	0.398	0.188	8	0.869
0.1	7	0.395	0.186	7	0.847	9	0.391	0.179	9	0.832
0.5	13	0.379	0.153	13	0.695	18	0.378	0.149	21	0.677
1	16	0.382	0.132	18	0.589	19	0.382	0.130	29	0.572
2	24	0.400	0.106	21	0.458	33	0.405	0.108	40	0.443
5	30	0.484	0.068	29	0.275	39	0.494	0.072	48	0.265
10	31	0.644	0.042	31	0.162	40	0.659	0.045	50	0.157
20	32	0.981	0.023	32	0.088	40	1.002	0.026	53	0.086
30	31	1.323	0.016	27	0.061	40	1.349	0.018	52	0.059
50	34	2.011	0.010	33	0.037	44	2.048	0.011	57	0.036
100	40	3.736	0.005	44	0.019	53	3.801	0.006	68	0.018

Table 3
Thermal slip coefficients calculated based on the LBE for the hard-sphere and Maxwellian molecules, and the coefficient obtained from the Shakhov kinetic model [38].

	Hard-sphere	Maxwellian	Shakhov model
σ_T	1.010	1.168	1.175

The numerical results are shown in Table 3. It is clear that there is a large difference (nearly 20%) between the LBE for the hard-sphere gas and the Shakhov model, but the difference between the LBE for the Maxwellian gas and the Shakhov model is small. This is probably because the collision frequencies in the LBE for Maxwellian molecules and the Shakhov model are constants, while that in the LBE for hard-sphere molecules is a function of the molecular velocity. This example shows that it is necessary to use the Boltzmann equation even in the near-continuum flow regime, and the SIS developed here is useful, for example, in assessing the accuracy of various kinetic gas–surface boundary conditions by comparing the numerical solutions for thermal transpiration flow with experimental data [41,42].

2.5. The most efficient scheme

In Sec. 2.4 we saw that the SIS for the LBE can be faster than the CIS by several orders of magnitude in the near-continuum regime. Now we look at the possibility of speeding up the convergence even more, without modifying the SIS too much. To this end, we penalize the linearized Boltzmann collision operator into the following form:

$$L = (L - NL_{BGK}) + NL_{BGK}, \tag{30}$$

where the constant N is a tuning parameter which affects the convergence rate.

With Eq. (20) replaced by Eq. (30), the diffusion-type equation (22) should be changed accordingly. Our numerical results for Poiseuille flow between two parallel plates show that, for a fixed δ, all synthetic schemes with different values of N converge to the same solution (with relative errors in flow rates less than 0.1%). However, the convergence rate varies with N. From the top row in Fig. 2 we see that in the free molecular regime all schemes have the same convergence rate, while in the transition regime the scheme with $N < 1$ ($N > 1$) converges slower (faster) than that with $N = 1$. The situation becomes complicated in the near-continuum regime: for hard-sphere molecules, the case with $N = 1.5$ converges fastest, followed by $N = 1$, 2, and 0.5. For Maxwell molecules, however, the cases with $N = 1.5$ and $N = 2$ have roughly the same fast convergence, followed by $N = 1$ and 0.5. Similar behaviors are observed for the thermal transpiration flow.

To further investigate the relationship between the convergence iteration step and N in the synthetic scheme, we fix $\delta = 100$ and vary N. The numerical results in the bottom row of Fig. 2 show that the fastest convergence is achieved when N is approximately 2 and 1.5 for Maxwell and hard-sphere molecules, respectively. This may be interpreted in terms of the average collision frequency. In the LBE, the equilibrium collision frequency ν_{eq} is in general a function of the molecular velocity. The average collision frequency,

$$\bar{\nu} = \int \nu_{eq}(\mathbf{v}) f_{eq}(\mathbf{v}) d\mathbf{v}, \tag{31}$$

varies between different intermolecular potentials even when the shear viscosity is the same. We found that for Maxwell and hard-sphere molecules, the average collision frequencies are 2.22 and 1.25 times larger than the rarefaction parameter,

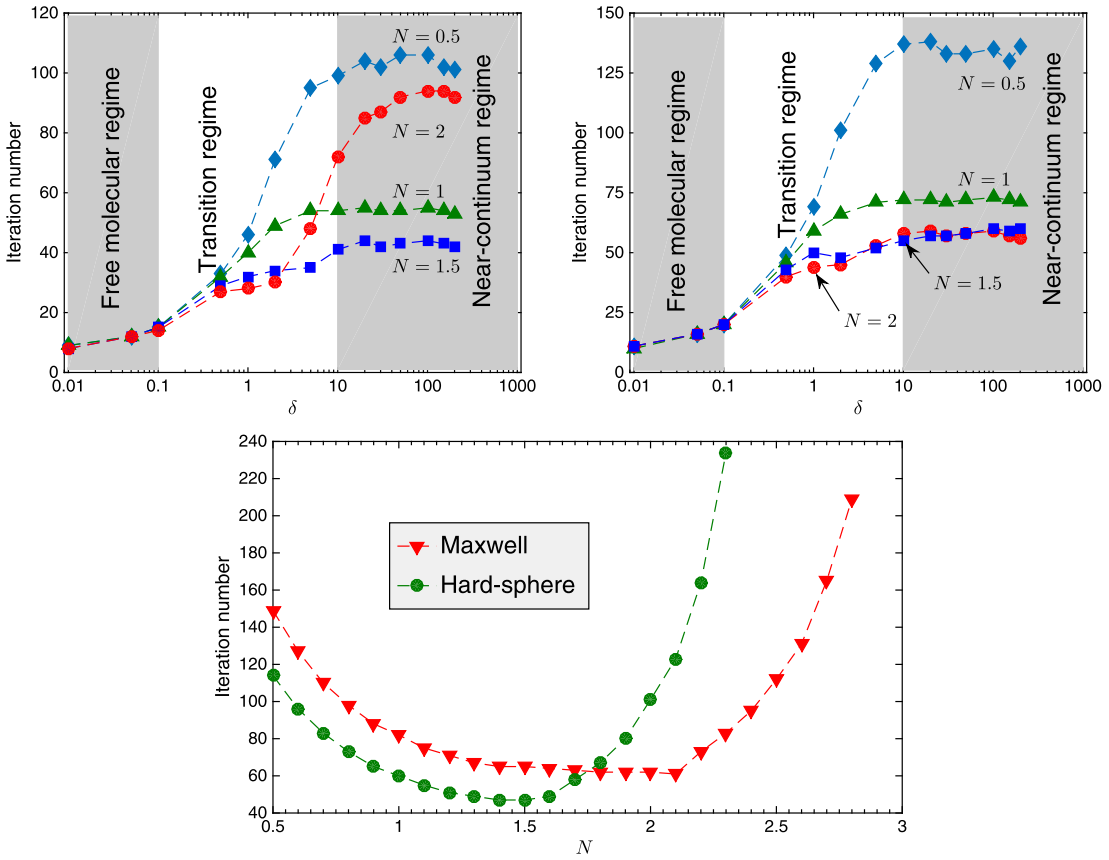

Fig. 2. Top row: iteration number versus the rarefaction parameter δ in the SIS (the convergence criterion is $\epsilon = 10^{-10}$) for Poiseuille flow between two parallel plates. Top left: hard-sphere molecules. Top right: Maxwell molecules. Bottom row: number of iterations to convergence versus N in the SIS when the rarefaction parameter is $\delta = 100$.

respectively—which are very close to the two values for the fastest convergence as seen in the bottom row of Fig. 2. Therefore, to achieve the best performance of the synthetic scheme we suggest using

$$N = \frac{\bar{\nu}}{\delta}, \tag{32}$$

which further reduces the iteration number by about 30% when compared to the case of $N = 1$.

2.6. Further benefit in using SIS

In addition to the significant speed-up of convergence, the SIS can also help to reduce the spatial resolution. It is well-known that in order to solve the kinetic equations the size of the spatial cells in the traditional discrete velocity method or the DSMC method should be smaller than the molecular mean free path, so that numerical results are reliable because the artificial viscosity is much smaller than the physical viscosity. In the SIS, the macroscopic flow velocity is obtained by solving the synthetic diffusion-type equation (22) which is asymptotic-preserving into the Navier–Stokes regime, so the spatial resolution can be relatively coarser.

To demonstrate this, we run the test case in Sec. 2.4 again, but the half spatial domain is instead divided into 10 uniform cells; for $\delta = 200$, this means that the spatial cell size is about 10 times larger than the molecular mean free path. Both the SIS and CIS on this coarse grid are compared to the reference solutions of Table 1. Since the mass flow rate in Poiseuille flow increases rapidly with δ, we study how the apparent gas permeability changes with the rarefaction parameter. Here, the apparent gas permeability, which is normalized by ℓ^2, is defined as

$$\kappa = \frac{\mathcal{M}_P}{\delta}. \tag{33}$$

Note that according to the Navier–Stokes equation with the no-slip velocity boundary condition, the flow velocity satisfies

$$\frac{\partial^2 U_3}{\partial {x_1}^2} = -\delta, \quad \text{with } U_3\left(x_1 = \pm\frac{1}{2}\right) = 0. \tag{34}$$

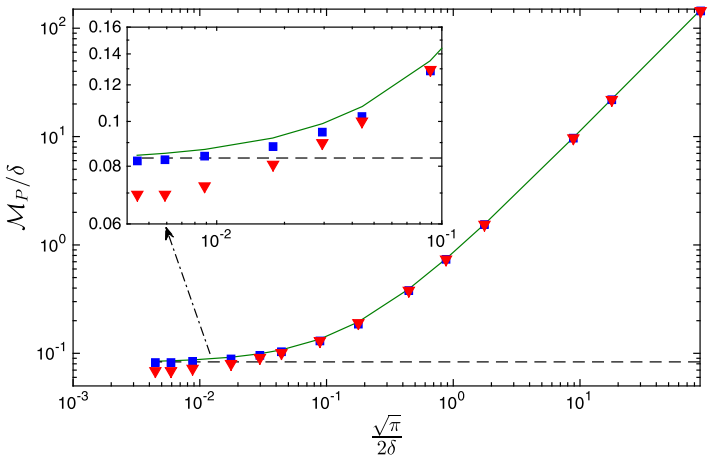

Fig. 3. The apparent gas permeability in the Poiseuille flow of a hard-sphere gas between two parallel plates. Solid lines: reference solution obtained from Table 1. Squares and triangles: the SIS and CIS solutions, respectively, of the LBE when the half spatial region is divided into 10 uniform sections. Dashed lines: the intrinsic permeability $\kappa = 1/12$, obtained from the Navier–Stokes equation with the no-slip boundary condition.

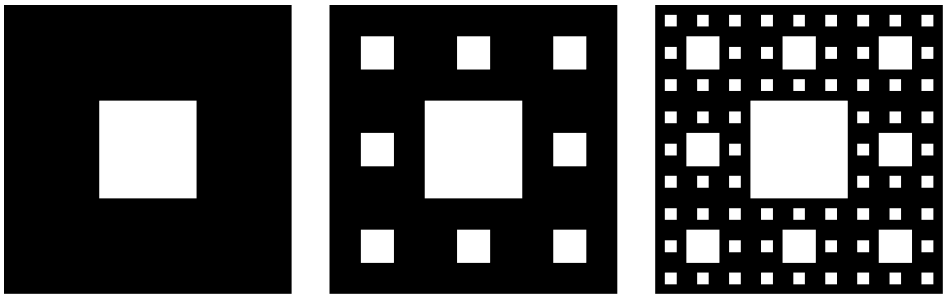

(a) Level 1 (b) Level 2 (c) Level 3

Fig. 4. The Sierpinski carpet generated at different levels of recursion. White regions represent the solid, while the gas can flow through the black regions.

Thus we have $U_3 = -(\delta/2)(x_1^2 - 1/4)$, and $\kappa = 1/12$; this permeability is also known as the "intrinsic" or "liquid" permeability. The apparent gas permeability is always larger than the intrinsic permeability, and increases with $1/\delta$ (or the Knudsen number).

Figure 3 shows the apparent gas permeability obtained for these different spatial resolutions over a wide range of the rarefaction parameter. It is clear that the SIS, even with a coarse spatial resolution, can yield good results. This proves that the SIS is asymptotic-preserving into the Navier–Stokes regime. The CIS results, however, have larger errors at large values of δ. For instance, when $\delta = 150$, the non-accelerated scheme underpredicts the apparent gas permeability by about 12.5%. This error continues to increases with δ: we have tested the BGK model for $\delta = 10^4$ and found that the relative error is about 62.5% [43].

3. SIS in multiscale problems

We now investigate the performance of the SIS in more complex geometries, where the problems are multiscale in the sense that the rarefaction parameter varies by several orders of magnitude due to different characteristic flow length scales, e.g. flow in a fractal geometry.

3.1. Rarefied gas flow through the Sierpinski carpet

We first consider the gas flow through a two-dimensional cross section described by the Sierpinski carpet, which can be generated through recursion. Beginning with a square, the square is cut into 9 congruent subsquares in a 3×3 grid, and the central subsquare is removed. The same procedure is then applied recursively to the remaining 8 subsquares. Resulting geometries after several levels of recursion are presented in Fig. 4.

Due to the symmetry, the one quarter of the level 1, 2, and 3 Sierpinski carpets are divided into 60×60, 90×90, and 135×135 uniform cells, respectively. The molecular velocity space is represented by $32 \times 32 \times 12$ discrete grids. We find that the iteration number, using $N = 1.5$ in Eq. (30) for a hard-sphere gas, is always less than 55 for each rarefaction parameter, when the relative error in the mass flow rate $\mathcal{M}_P$ between two consecutive iterations is less than 10^{-5}.

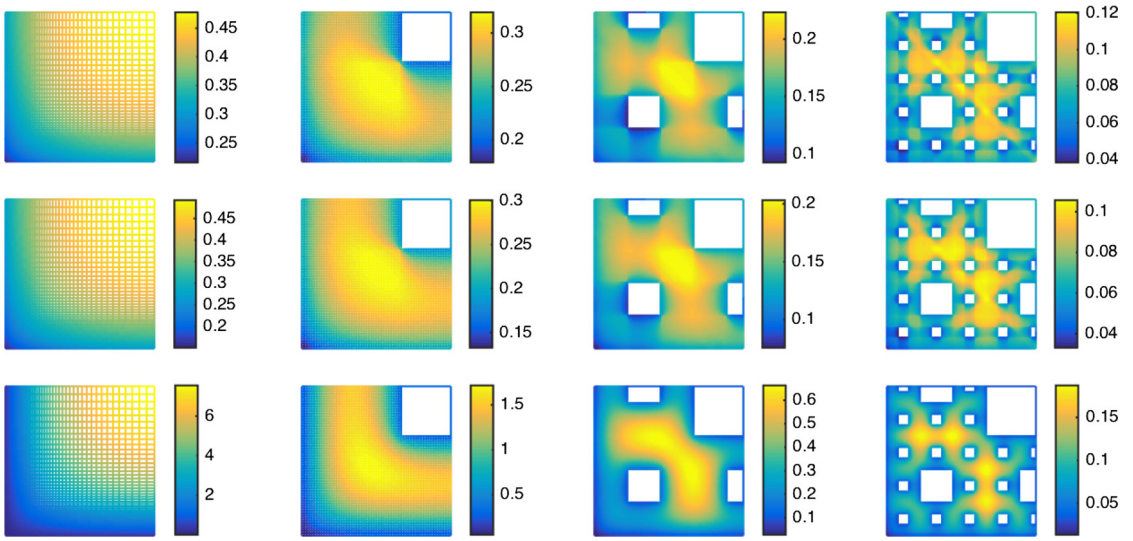

Fig. 5. Velocity contours in the Poiseuille flow of a hard-sphere gas through the Sierpinski carpets generated at different levels of recursion (from the left column to the right, the recursion levels are 0, 1, 2, and 3, respectively), when $\delta = 1$ (top row), 10 (middle row), and 100 (bottom row). Due to symmetry, only one quarter flow domain is shown. The gas flows into the page.

Figure 5 displays the velocity contours at different geometries and for different rarefaction parameters, where the characteristic flow length ℓ is chosen to be the side length of the largest square. When there is no solid inside the largest square (first column in Fig. 5), the maximum velocity is at the center of the domain. When there are some solids inside the largest square, and when δ is small, it seems that large flow velocities are located near the central regions. However, when δ is large, large flow velocities are localized between the smallest squares that are offset from other larger squares nearby, instead of in the central region of the carpets. This may be seen clearly in the flow in the Sierpinski carpet of level 3 (the right bottom of Fig. 5).

Figure 6 shows the mass and heat flow rates in the Poiseuille flow of the hard-sphere gas through the Sierpinski carpet. The Knudsen minimum in the mass flow rate can be seen, however, the location of the minimum $\mathcal{M}_P$ shifts towards larger values of δ as the recursion level of the Sierpinski carpet increases. This is because, in the calculation of δ according to Eq. (12), the characteristic flow length ℓ is chosen to be the side length of the largest square, which is larger than, say, the smallest side length of the solids near which the flow velocity is maximum. As the recursion level increases, the porosity (the void area fraction) of the Sierpinski carpet decreases, so the flow rates decrease. We also plot in Fig. 6 the thermomolecular pressure difference exponent, which is an important parameter determining the performance of a Knudsen pump. The exponent always increases with decreasing δ and approaches the value of 0.5 when $\delta \to 0$ if the diffuse gas–surface boundary condition is used [40]. This also indicates the correctness of our numerical simulations.

3.2. Rarefied gas flow through random structures

We also consider the gas flow through two-dimensional porous media, where the porosity is 0.6. The first porous medium is generated by adding circular solids of different radii randomly to a square. The radius ratio of the largest disc to the smallest is 10. The square is then divided into 200×200 uniform cells, and the discs are approximated by the "staircase", as visualized in Fig. 7(a). The second porous medium, shown in Fig. 7(b), also consisting of 200×200 uniform cells, is generated by the quartet structure generation set [44].

Following the numerical simulations, velocity contours are displayed in Fig. 8 for the free molecular and near-continuum flow regimes, while the mass and heat flow rates are shown in Fig. 9 from the free molecular to near-continuum flow regimes. It is interesting to note that, in the free molecular flow regime, the mass flow rates in the two random porous media are nearly the same. However, in the near-continuum regime, the mass flow rate of the porous medium consisting of random squares is about twice that in disc medium. This research may find applications in shale gas extraction.

4. A special case: SIS in polar coordinates

The SIS developed above for the LBE works well in Cartesian coordinates, for rarefied gas flows through general cross sections. For flows through circular cross sections, the use of polar coordinates can reduce the computational cost significantly, as previously demonstrated in the SIS for the McCormack kinetic model [22,24]. However, for the LBE, the velocity space cannot be represented in polar coordinates as that of the McCormack kinetic model, since the molecular velocity along the flow direction cannot be integrated due to the nonlinear structure of the Boltzmann equation. Therefore, the SIS for the

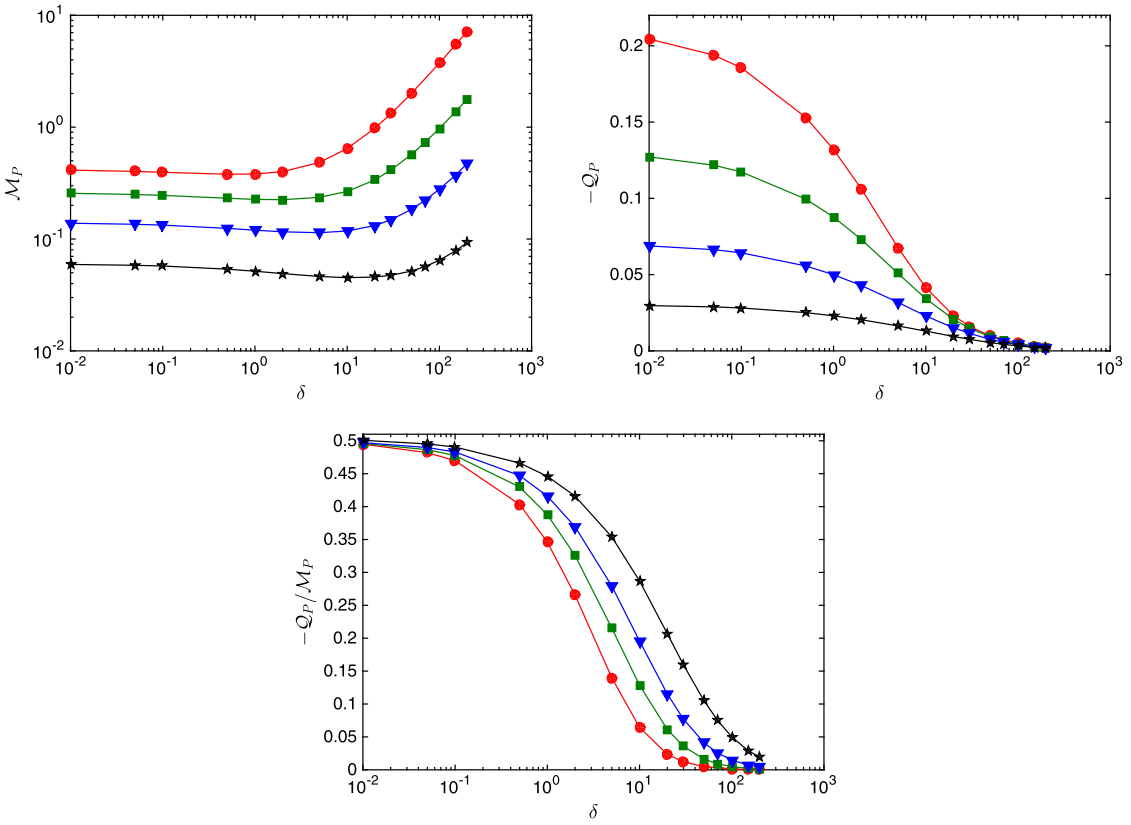

Fig. 6. Mass flow rate $\mathcal{M}_P$, heat flow rate $\mathcal{Q}_P$, and the thermomolecular pressure difference exponent $-\mathcal{Q}_P/\mathcal{M}_P$ in the Poiseuille flow of a hard-sphere gas through the Sierpinski carpets. Circles, squares, triangles, and pentagrams represent the results for the Sierpinski carpets generated at recursion level 0, 1, 2, and 3, respectively.

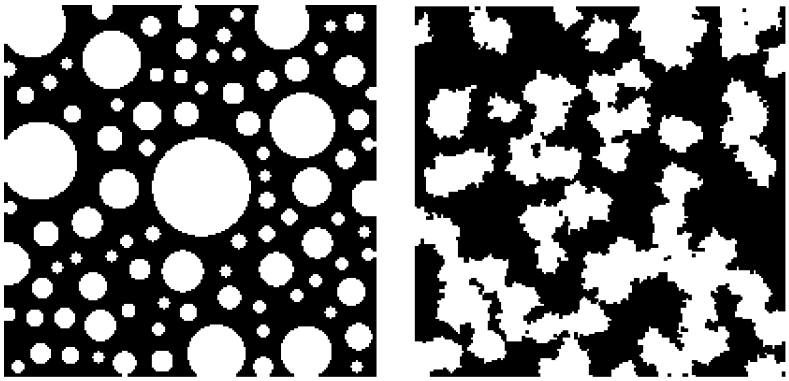

Fig. 7. Porous media with a porosity of 0.6, consisting of (a) discs of random position and radius, and (b) islands of different size and shape composed of multiple small squares. White regions represent the solid, while the gas can flow through the black regions.

LBE will be developed in polar coordinates for spatial variables, while the three-dimensional molecular velocity space is represented by cylindrical coordinates.

We consider Poiseuille flow along a pipe as an example, where the axis of the pipe is along the x_3 direction, and its cross section is located in the x_1–x_2 plane. The spatial coordinates are normalized by the radius of the tube. Introducing the transformation $x_1 = r\cos\theta$, $x_2 = r\sin\theta$, $v_1 = v_r\cos\theta$, $v_2 = v_r\sin\theta$, and defining the VDF $h = h(r, \theta, v_r, v_3)$ in cylindrical (molecular velocity)-polar (space) coordinates $v_r \in [0, +\infty)$, $\theta \in [0, 2\pi]$, $v_z \in (-\infty, \infty)$, and $r \in [0, 1]$, the LBE can be written as:

$$v_1\frac{\partial h}{\partial r} - \frac{v_2}{r}\frac{\partial h}{\partial \theta} = L(h, f_{eq}) + v_3 f_{eq}. \tag{35}$$

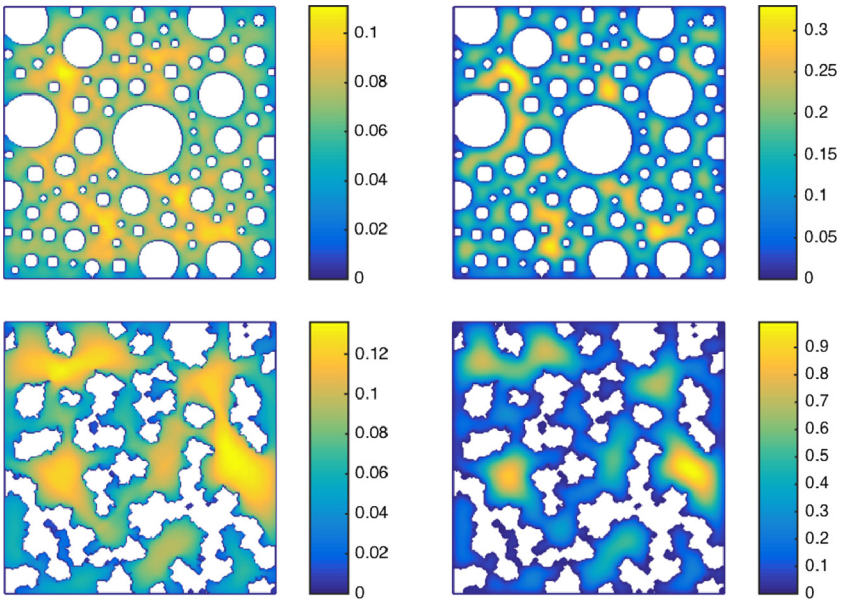

Fig. 8. Velocity contours in the Poiseuille flow of a hard-sphere gas through the two random porous media in Fig. 7, when $\delta = 0.01$ (left column) and 300 (right column). The gas flows into the page.

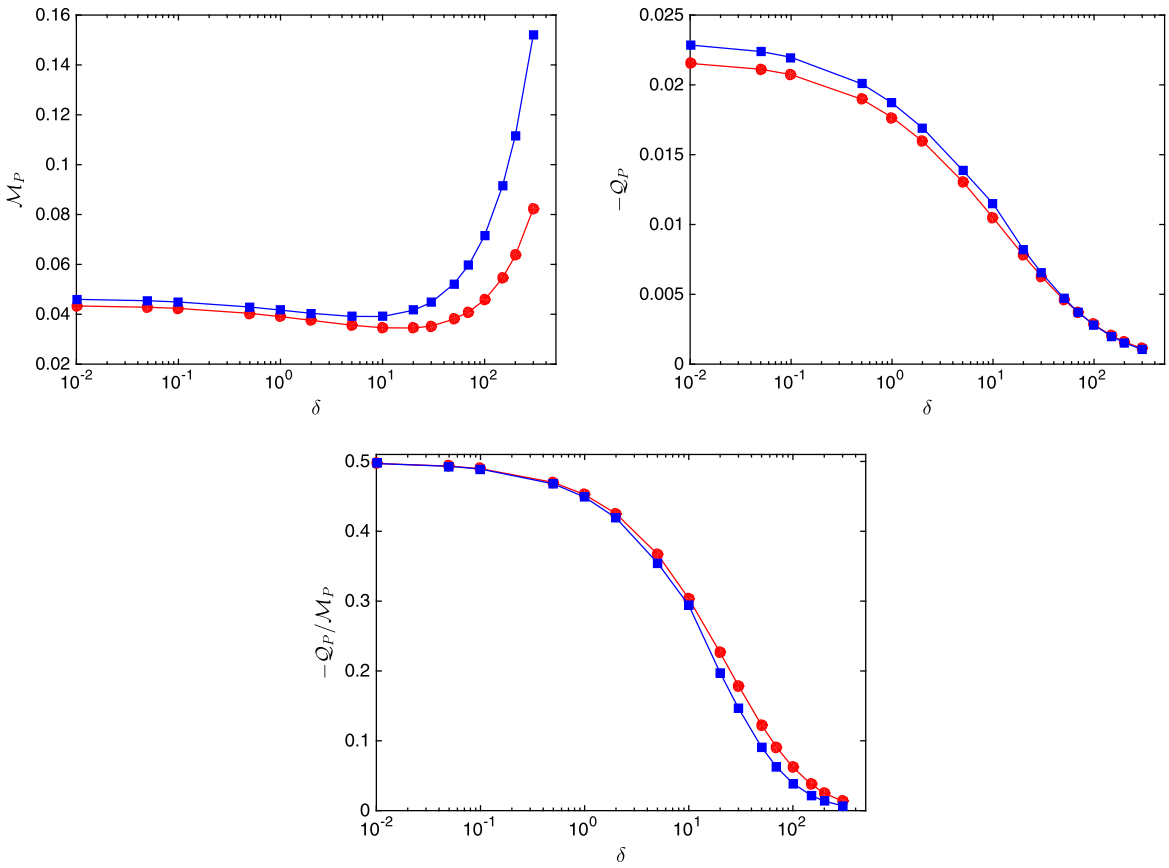

Fig. 9. Mass flow rate $\mathcal{M}_P$, heat flow rate $\mathcal{Q}_P$, and the thermomolecular pressure difference exponent $-\mathcal{Q}_P/\mathcal{M}_P$ in the Poiseuille flow of a hard-sphere gas through the porous media of Fig. 7 consisting of random discs (circles) and islands (squares).

Table 4
Mass and heat flow rates in Poiseuille flow of hard-sphere and Maxwell molecules along a tube of circular cross section, as well as the number of iterations (Itr) to reach the convergence criterion $\epsilon = 10^{-10}$ in the SIS. We choose $N = 1$ in Eq. (40).

δ	Hard-sphere molecules			Maxwell molecules		
	Itr	$\mathcal{M}_P$	$-\mathcal{Q}_P$	Itr	$\mathcal{M}_P$	$-\mathcal{Q}_P$
0.0	3	0.752	0.376	3	0.752	0.376
0.01	6	0.736	0.362	7	0.731	0.355
0.1	11	0.699	0.318	15	0.693	0.307
0.5	24	0.691	0.247	34	0.692	0.244
1	33	0.724	0.202	48	0.732	0.205
5	46	1.160	0.082	62	1.179	0.091
10	45	1.766	0.046	60	1.786	0.052
20	49	3.004	0.024	65	3.024	0.028
30	47	4.247	0.017	63	4.269	0.019
50	45	6.745	0.010	60	6.765	0.012
100	42	12.99	0.005	56	13.01	0.006

To construct the SIS in polar coordinates, a diffusion-type equation for the flow velocity $U_3(r)$ should be derived. Since the Laplace operator $\partial^2 U_3/\partial x_1^2 + \partial^2 U_3/\partial x_2^2$ in Eq. (22) can be rewritten as $\frac{1}{r}\frac{\partial}{\partial r}\left(r\frac{\partial U_3}{\partial r}\right)$, our goal is to construct the diffusion-type equation in the following form:

$$\frac{1}{r}\frac{\partial}{\partial r}\left(r\frac{\partial U_3}{\partial r}\right) = -N\delta + \text{high-order terms}, \tag{36}$$

by taking the velocity moment of the LBE (35).

Multiplying Eq. (35) by $2v_3$ and integrating over the molecular velocity space, we obtain the equation for the shear stress $P_{rz} = \int 2v_3 v_1 h d\mathbf{v} = \int 2v_3 v_r^2 \cos\theta h dv_r dv_3 d\theta$ as

$$\frac{1}{r}\frac{\partial}{\partial r}(rP_{rz}) = 1. \tag{37}$$

Multiplying Eq. (35) by $v_3 v_1$, penalizing the linearized Boltzmann collision operator in the form of Eq. (30), and integrating over the molecular velocity space, we obtain

$$\frac{\partial}{\partial r}\int v_3 v_1^2 h d\mathbf{v} + \frac{1}{r}\int v_3(v_1^2 - v_2^2) h d\mathbf{v} = -\frac{N\delta P_{rz}}{2} + \int v_3 v_1 (L - NL_{BGK}) d\mathbf{v}, \tag{38}$$

which is simplified, with the help of Eq. (37), into

$$\frac{1}{r}\frac{\partial}{\partial r}\left[r\frac{\partial}{\partial r}\int 2v_3 v_1^2 h d\mathbf{v} + \int 2v_3(v_1^2 - v_2^2) h d\mathbf{v} - r\int 2v_3 v_1 (L - NL_{BGK}) d\mathbf{v}\right] = -N\delta. \tag{39}$$

If we express $\int 2v_3 v_1^2 h d\mathbf{v} = \int v_3(2v_1^2 - 1) h d\mathbf{v} + U_3$, the diffusion-type equation in the form of Eq. (36) can be derived. But for practical numerical calculations, the following first-order ordinary differential equation for the flow velocity is desirable:

$$\frac{\partial U_3}{\partial r} = -\frac{N\delta r}{2} - \frac{\partial}{\partial r}\int v_3(2v_1^2 - 1) h d\mathbf{v} - \frac{1}{r}\int 2v_3(v_1^2 - v_2^2) h d\mathbf{v} + \int 2v_3 v_1 (L - NL_{BGK}) d\mathbf{v}. \tag{40}$$

In the numerical simulation, the spatial coordinate r is discretized into 150 nonuniform points, with most of the points located near the pipe surface $r = 1$. Due to symmetry, the truncated velocity $v_r \in (0, 4)$ is discretized into 64 nonuniform points, with most of the points located near $v_r = 0$, while $\theta \in [0, \pi]$ and $v_3 \in (0, 6)$ are discretized into 40 and 12 uniform points, respectively. The linearized Boltzmann collision operator is approximated by the fast spectral method: first, the spectrum of the VDF is calculated by Fourier transform from the cylindrical molecular velocity space to the Cartesian frequency space. Second, the fast spectral method [28] is applied to find the spectrum of the linearized Boltzmann collision operator in the Cartesian coordinate. Finally, the inverse Fourier transform is used to find the collision operator in the cylindrical space. The SIS in polar coordinate is implemented in the following three steps: first, as usual, Eq. (35) is solved by the implicit iterative scheme, with the spatial derivatives being approximated by the second-order upwind finite difference. Then, Eq. (40), which is used to expedite convergence to the steady-state solution, is also solved using the second-order upwind finite difference, where the boundary condition of $U_3(r)$ at $r = 1$ is calculated from the VDF obtained in the first step. Finally, having obtained $U_3(r)$ from Eq. (40), a correction in the VDF is performed, see Eq. (24).

Our numerical results for mass and heat flow rates in Poiseuille flow of a hard-sphere gas through a pipe are summarized in Table 4. It can be seen that, as for rarefied gas flows between two parallel plates and in rectangular cross sections, the SIS in the polar coordinates is also very efficient.

5. SIS for the LBE for gas mixtures

In this section we develop a SIS for the LBE for binary gas mixtures. For simplicity, only Poiseuille flow is considered, but the method can be generalized to flows driven by temperature and concentration gradients.

Let f_A and f_B be, respectively, the VDFs of gas components A and B with molecular masses m_A and m_B, and molar fractions χ_A and $\chi_B = 1 - \chi_A$. Introducing the equilibrium VDF (in which the velocity is normalized by the most probable speed $v_{mA} = \sqrt{2k_B T_0/m_A}$ of component A [35]):

$$f_{\alpha,eq}(\mathbf{v}) = \chi_\alpha \left(\frac{m_\alpha}{\pi m_A}\right)^{3/2} \exp\left(-\frac{m_\alpha |\mathbf{v}|^2}{2m_A}\right), \quad \alpha = \text{A or B}, \tag{41}$$

and expressing the VDF in the form $f_\alpha = f_{\alpha,eq} + h_\alpha$, where h_α are perturbed VDFs satisfying $|h_\alpha / f_{\alpha,eq}| \ll 1$, the LBE for h_α is

$$v_1 \frac{\partial h_\alpha}{\partial x_1} + v_2 \frac{\partial h_\alpha}{\partial x_2} = L_\alpha + S_\alpha, \tag{42}$$

with the linearized Boltzmann collision operators $L_\alpha = \sum_{\beta=1,2} Q_{\alpha\beta}(f_{\alpha,eq}, h_\beta) + Q_{\alpha\beta}(h_\alpha, f_{\beta,eq})$, where the details of $Q_{\alpha\beta}$ can be found in Ref. [35]. The source term for Poiseuille flow is

$$S_\alpha = -X_P v_3 f_{\alpha,eq}, \tag{43}$$

and again we take $X_P = -1$.

When the perturbed VDFs are known, the flow velocity normalized by v_{mA} is calculated as $U_\alpha = \int h_\alpha v_3 d\mathbf{v}/\chi_\alpha$, shear stresses normalized by the total gas pressure p_0 are $P_{\alpha 13} = 2m_\alpha \int h_\alpha v_1 v_3 d\mathbf{v}/m_A$ and $P_{\alpha 23} = 2m_\alpha \int h_\alpha v_2 v_3 d\mathbf{v}/m_A$, and the heat flux normalized by $p_0 v_{mA}$ is $q_\alpha = \int \left(m_\alpha |\mathbf{v}|^2/m_A - 5/2\right) v_3 h d\mathbf{v}$. The dimensionless mass flow rate $\mathcal{M}$ and heat flow rate $\mathcal{Q}$, normalized by the most probable speed of the gas mixture, are calculated as

$$\begin{aligned} \mathcal{M}_\alpha &= \frac{1}{A}\sqrt{\frac{m}{m_A}} \iint U_\alpha dx_1 dx_2, \\ \mathcal{Q}_\alpha &= \frac{1}{A}\sqrt{\frac{m}{m_A}} \iint q_\alpha dx_1 dx_2, \end{aligned} \tag{44}$$

where $m = \chi_A m_A + (1 - \chi_A) m_B$ is the average molecular mass of the mixture.

5.1. The synthetic scheme for a gas mixture

As emphasized above, the relation $\partial P_{13}/\partial x_1 + \partial P_{23}/\partial x_2 = 1$ is important in developing the SIS. For binary mixtures, this relation still holds, but now shear stresses are replaced by mixture shear stresses, i.e. $P_{13} = P_{A13} + P_{B13}$ and $P_{23} = P_{A23} + P_{B23}$. This poses an additional difficulty.

Following the basic steps in developing the synthetic equation, we obtain the following two equations for the flow velocity of each component:

$$\begin{aligned} \chi_\alpha \left(\frac{\partial^2 U_\alpha}{\partial x_1^2} + \frac{\partial^2 U_\alpha}{\partial x_2^2}\right) &= 2\frac{\partial}{\partial x_1} \int v_1 v_3 L_\alpha d\mathbf{v} + 2\frac{\partial}{\partial x_2} \int v_2 v_3 L_\alpha d\mathbf{v} \\ &\quad - \frac{1}{4}\left(\frac{\partial^2 F^\alpha_{2,0,1}}{\partial x_1^2} + 2\frac{\partial^2 F^\alpha_{1,1,1}}{\partial x_1 \partial x_2} + \frac{\partial^2 F^\alpha_{0,2,1}}{\partial x_2^2}\right), \end{aligned} \tag{45}$$

where $F^\alpha_{m,n,l} = \int h_\alpha H_m(v_1) H_n(v_2) H_l(v_3) d\mathbf{v}$.

To obtain diffusion-type equations which recover the Stokes equation (an important step, guaranteeing fast convergence) in the hydrodynamic regime, we rewrite the linearized collision operator as[2]:

$$L_\alpha = (L_\alpha + N_\alpha \delta h_\alpha) - N_\alpha \delta h_\alpha, \tag{46}$$

where N_α are two constants, and let $2\int v_1 v_3 L_\alpha d\mathbf{v} = \int v_1 v_3 (L_\alpha + N_\alpha \delta h_\alpha) d\mathbf{v} - N_\alpha \delta m_A P_{\alpha 13}/m_\alpha$ and $2\int v_2 v_3 L_\alpha d\mathbf{v} = \int v_2 v_3 (L_\alpha + N_\alpha \delta h_\alpha) d\mathbf{v} - N_\alpha \delta m_A P_{\alpha 23}/m_\alpha$. Then, for component B, Eq. (45) is transformed to

[2] This is because the linearized Boltzmann collision operator for single-species gases can also be penalized in the form $L = (L + N\delta h) - N\delta h$, instead of the form given in Eq. (30). The virtue of Eq. (46) is that the resulting diffusion-type equations are very simple (compared to those in Refs. [37,45] for the McCormack kinetic model), but without any loss of efficiency of the SIS.

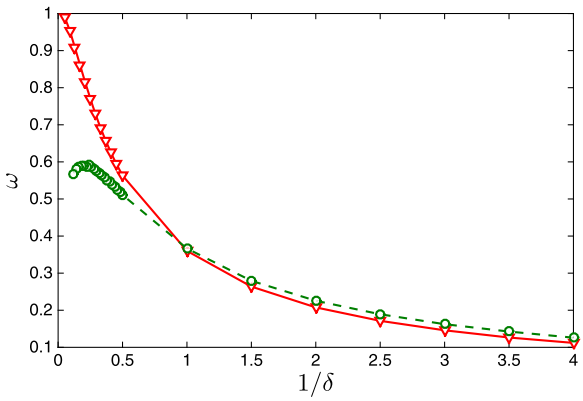

Fig. 10. Eigenvalue ω versus the inverse rarefaction parameter $1/\delta$ for the SIS (circles) and the CIS (triangles) for the LBE of an equimolar Ne–Ar mixture.

$$\chi_B\left(\frac{\partial^2 U_B}{\partial x_1^2}+\frac{\partial^2 U_B}{\partial x_2^2}\right)=-N_B\delta\frac{m_A}{m_B}\left(\frac{\partial P_{B13}}{\partial x_1}+\frac{\partial P_{B23}}{\partial x_2}\right)-\frac{1}{4}\left(\frac{\partial^2 F^B_{2,0,1}}{\partial x_1^2}+2\frac{\partial^2 F^B_{1,1,1}}{\partial x_1\partial x_2}+\frac{\partial^2 F^B_{0,2,1}}{\partial x_2^2}\right)$$
$$+2\frac{\partial}{\partial x_1}\int v_1 v_3(L_B-N_B\delta f_B)d\mathbf{v}+2\frac{\partial}{\partial x_2}\int v_2 v_3(L_B-N_B\delta f_B)d\mathbf{v}, \tag{47}$$

while for component A, by using the relation $\partial P_{13}/\partial x_1+\partial P_{23}/\partial x_2=1$ with $P_{13}=P_{A13}+P_{B13}$ and $P_{23}=P_{A23}+P_{B23}$, Eq. (45) is transformed to

$$\chi_A\left(\frac{\partial^2 U_A}{\partial x_1^2}+\frac{\partial^2 U_A}{\partial x_2^2}\right)=N_A\delta\left(\frac{\partial P_{B13}}{\partial x_1}+\frac{\partial P_{B23}}{\partial x_2}-1\right)-\frac{1}{4}\left(\frac{\partial^2 F^A_{2,0,1}}{\partial x_1^2}+2\frac{\partial^2 F^A_{1,1,1}}{\partial x_1\partial x_2}+\frac{\partial^2 F^A_{0,2,1}}{\partial x_2^2}\right)$$
$$+2\frac{\partial}{\partial x_1}\int v_1 v_3(L_A-N_A\delta f_A)d\mathbf{v}+2\frac{\partial}{\partial x_2}\int v_2 v_3(L_A-N_A\delta f_A)d\mathbf{v}. \tag{48}$$

We therefore propose the SIS for the LBE for binary gas mixtures: while the VDFs in Eq. (42) are first solved by the CIS [35], flow velocities are updated according to diffusion-type equations (47) and (48). Then the VDFs are corrected in a way similar to Eq. (24). Note that the fastest convergence is achieved when

$$N_\alpha=\frac{\int \nu_{\alpha,eq}(\mathbf{v})f_{\alpha,eq}(\mathbf{v})d\mathbf{v}}{\delta\chi_\alpha}, \tag{49}$$

where $\nu_{\alpha,eq}$ is the equilibrium collision frequency of the α-component.

The present SIS is readily generalized to multiple-species gas mixtures. Suppose there are j gas components; for the velocity of the first component, the term $\partial P_{B13}/\partial x_1+\partial P_{B23}/\partial x_2$ in the diffusion-type equation (48) can be replace by $\sum_{i=2}^{j}(\partial P_{i13}/\partial x_1+\partial P_{i23}/\partial x_2)$, while the diffusion-type equations for the flow velocities of the other components remain the same as Eq. (47), i.e. by replacing B with the component index i. This method can also be applied to the McCormack kinetic equation [25] for multiple gas mixture, by simply replacing L_α in Eqs. (47) and (48) with that in the McCormack model; the resulting diffusion-type equations will be much simpler than those in Refs. [37,45].

5.2. Convergence analysis

To show the efficiency of the proposed SIS for binary gas mixtures, we calculate the eigenvalue of the iteration as a function of the inverse rarefaction parameter. The numerical procedure is essentially the same as that in Sec. 2.3 for single-species gases. Fig. 10 shows the eigenvalue of both the SIS and CIS for an equimolar Ne–Ar mixture, where Ne and Ar are treated as hard-sphere molecules with a molecular diameter ratio of 0.711. It is clear that the SIS is superior to the CIS at large values of the rarefaction parameter. Also, when compared to the SIS for a single-species hard-sphere gas, the synthetic scheme for a binary gas mixture has roughly the same maximum eigenvalue, i.e. $\omega\simeq 0.6$. So it is expected that the synthetic scheme for a binary gas mixture will be as efficient as that for a single-species gas. It is also interesting to note that at small values of δ the eigenvalue of the SIS is slightly higher than that of the CIS; the reason for this is not clear. However, this does not affect the efficiency of the SIS because at small values of δ both the SIS and CIS converge rapidly, i.e. within a small number of iterations.

5.3. Numerical simulations of Poiseuille flow

Following the convergence analysis above, numerical simulations are now conducted for the Poiseuille flow of a Ne–Ar mixture between two parallel plates. First, the hard-sphere molecular potential is considered. Table 5 shows the mass and

Table 5
Mass and heat flow rates in Poiseuille flow of Ne–Ar gas mixtures between two parallel plates, as well as the number of iterations (Itr) to reach the convergence criterion $\epsilon = 10^{-10}$ in the SIS. The LBE with the hard-sphere model is used.

δ	$\chi_{Ne} = 0.1$					$\chi_{Ne} = 0.5$					$\chi_{Ne} = 0.9$				
	Itr	$\mathcal{M}_{Ne}$	$\mathcal{M}_{Ar}$	$-\frac{\mathcal{Q}_{Ne}}{\chi_{Ne}}$	$-\frac{\mathcal{Q}_{Ar}}{\chi_{Ar}}$	Itr	$\mathcal{M}_{Ne}$	$\mathcal{M}_{Ar}$	$-\frac{\mathcal{Q}_{Ne}}{\chi_{Ne}}$	$-\frac{\mathcal{Q}_{Ar}}{\chi_{Ar}}$	Itr	$\mathcal{M}_{Ne}$	$\mathcal{M}_{Ar}$	$-\frac{\mathcal{Q}_{Ne}}{\chi_{Ne}}$	$-\frac{\mathcal{Q}_{Ar}}{\chi_{Ar}}$
0.01	9	2.131	1.416	0.999	0.639	9	1.858	1.227	0.861	0.544	9	1.547	1.016	0.705	0.440
0.05	12	1.593	1.071	0.720	0.459	13	1.393	0.936	0.619	0.391	13	1.167	0.787	0.506	0.316
0.1	15	1.386	0.951	0.607	0.391	15	1.218	0.840	0.522	0.334	16	1.030	0.717	0.428	0.272
0.5	31	1.005	0.766	0.372	0.251	32	0.912	0.709	0.323	0.218	32	0.808	0.647	0.269	0.180
1	38	0.909	0.744	0.284	0.196	38	0.846	0.707	0.248	0.170	35	0.773	0.666	0.208	0.141
2	47	0.879	0.776	0.204	0.142	47	0.841	0.756	0.179	0.123	43	0.794	0.730	0.151	0.102
5	52	1.016	0.968	0.115	0.080	48	1.002	0.964	0.101	0.068	54	0.977	0.949	0.085	0.056
10	51	1.371	1.346	0.067	0.045	47	1.367	1.348	0.058	0.039	62	1.352	1.337	0.049	0.031
20	51	2.153	2.141	0.036	0.024	46	2.155	2.145	0.031	0.021	84	2.145	2.137	0.026	0.017
30	50	2.955	2.946	0.024	0.017	45	2.958	2.951	0.021	0.014	89	2.950	2.943	0.018	0.012
50	49	4.570	4.565	0.015	0.010	45	4.574	4.569	0.013	0.009	94	4.568	4.562	0.011	0.007
100	49	8.624	8.620	0.008	0.006	44	8.625	8.622	0.007	0.005	98	8.623	8.614	0.007	0.004

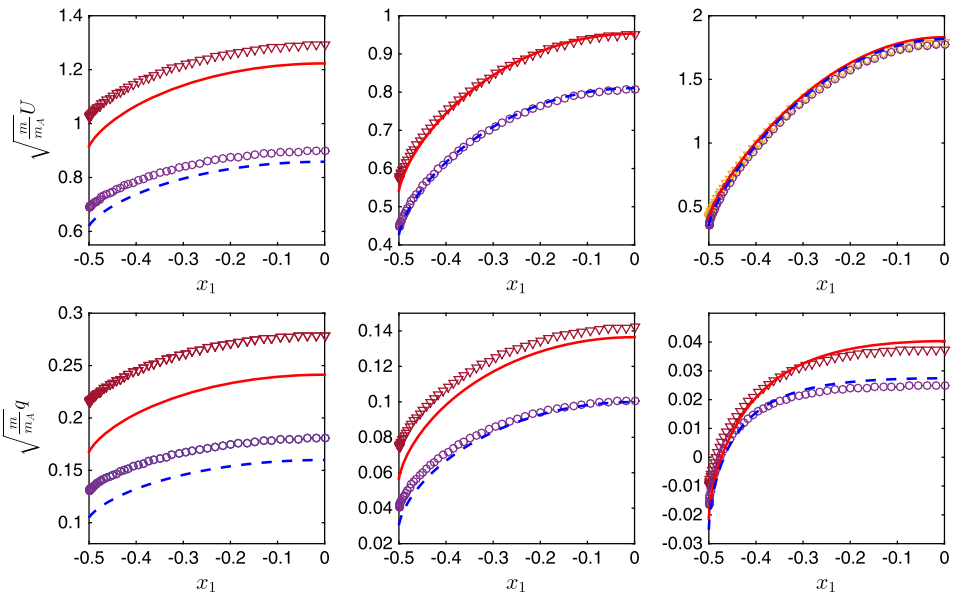

Fig. 11. Velocity (top row) and heat flux (bottom row) profiles in the Poiseuille flow of an equimolar Ne–Ar mixture between two parallel plates, where $\delta = 0.1,\ 1,$ and 10 in the left, middle, and right columns, respectively. Triangles and circles are the profiles of Ne and Ar, respectively, obtained from the LBE with the hard-sphere model, while solid and dashed lines are the corresponding profiles using the Lennard–Jones potential.

heat flow rates of each component over a wide range of gas rarefaction, for a molar fraction of Ne of 0.1, 0.5, and 0.9. From this table we see that the SIS is efficient, since convergence is reached within 100 iterations when $N_\alpha = 1$; when using $N_\alpha = 1.5$ in Eqs. (47) and (48), converged solutions can be obtained within 50 iterations. Such an efficient method enables the study of the flow dynamics over the whole range of gas rarefaction.

In the free molecular and transition regimes, the mass flow rate of the lighter species is always higher than that of the heavier species; however, in the near-continuum regime the mass flow rates are the same for both gas components. When compared to the results in Table 1 we see that the difference in the mass flow rates is within 1% in the near-continuum regime. A comparison of velocity and heat flux profiles in different flow regimes is presented in Fig. 11, which shows that the difference between the velocity profiles of each component is reduced as the rarefaction parameter increases. As δ increases, the difference between the heat fluxes further normalized by the molar fraction of each component also decreases, but in the near-continuum limit the heat flux of Ne is roughly $\sqrt{2}$ times that of Ar, while the difference in the mass flow rate goes to zero.

We have also simulated for the first time the Ne–Ar mixture flow based on the LBE for Lennard–Jones potentials, where the fast spectral approximation of the Boltzmann collision operator is described in Ref. [30]. The influence of the molecular model on the velocity and the heat flux profiles is shown in Fig. 11: the hard-sphere model overestimates the velocity and the heat flux in the free-molecular regime, but in the transition and near-continuum regimes the differences between the two molecular models reduce as δ increases. This is in good agreement with observations of the single-species case [29,30].

Figure 12 shows the mass and heat flow rates as a function of the rarefaction parameter. The two flow rates obtained from the LBE with Lennard–Jones potentials are both smaller than that for the hard-sphere model when $\delta < 1$ (e.g. when

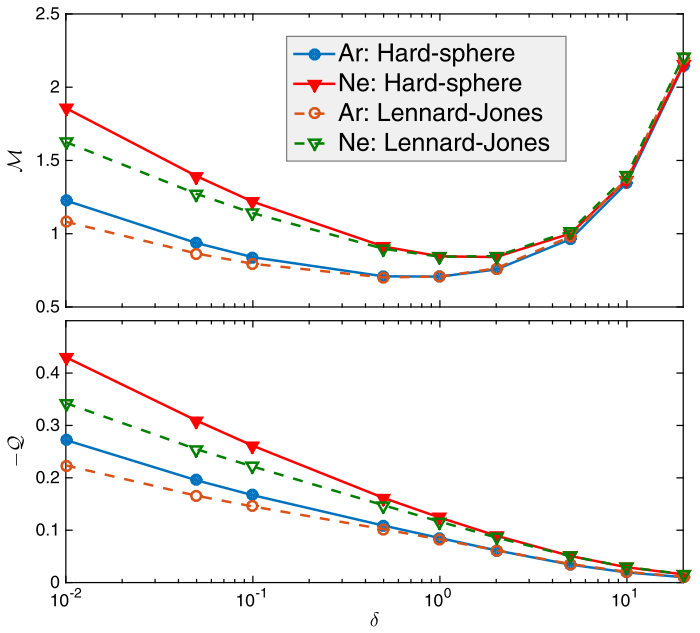

Fig. 12. A comparison between the Lennard–Jones and hard-sphere potentials: mass flowrate (top) and heat flow rate (bottom) profiles in the Poiseuille flow of an equimolar Ne–Ar mixture between two parallel plates.

Table 6
Mass and heat flow rates in Poiseuille flow of an equimolar Ne–Ar gas mixture along channels of rectangular cross section, of aspect ratios one and two, as well as the number of iterations (Itr) needed to reach the convergence criterion $\epsilon = 10^{-7}$ in the SIS. $N_\alpha = 1.5$ is adopted in Eqs. (47) and (48), and the LBE with the hard-sphere model is used.

δ	Aspect ratio 1					Aspect ratio 2				
	Itr	$\mathcal{M}_{Ne}$	$\mathcal{M}_{Ar}$	$-2\mathcal{Q}_{Ne}$	$-2\mathcal{Q}_{Ar}$	Itr	$\mathcal{M}_{Ne}$	$\mathcal{M}_{Ar}$	$-2\mathcal{Q}_{Ne}$	$-2\mathcal{Q}_{Ar}$
0.01	5	0.506	0.358	0.251	0.177	5	0.692	0.490	0.343	0.241
0.05	5	0.493	0.349	0.241	0.167	6	0.669	0.474	0.324	0.224
0.1	6	0.483	0.344	0.232	0.160	7	0.653	0.466	0.309	0.212
0.5	11	0.452	0.338	0.195	0.134	13	0.604	0.459	0.249	0.170
1	13	0.441	0.347	0.170	0.117	16	0.589	0.475	0.210	0.144
2	17	0.442	0.373	0.139	0.096	19	0.597	0.518	0.164	0.112
5	19	0.497	0.459	0.091	0.061	20	0.699	0.659	0.101	0.067
10	19	0.630	0.610	0.057	0.038	21	0.926	0.904	0.060	0.040
20	23	0.928	0.917	0.032	0.021	23	1.417	1.406	0.033	0.022
30	23	1.235	1.228	0.022	0.015	23	1.920	1.913	0.023	0.015
50	25	1.856	1.852	0.014	0.009	25	2.932	2.929	0.014	0.009
100	30	3.416	3.416	0.007	0.005	30	5.474	5.474	0.007	0.005

$\delta = 0.01$, the mass flow rates are about 15% smaller, while the heat flow rates are about 25% smaller). This situation is reversed for the mass flow rate, but results for the two different molecular models are nearly indistinguishable when $\delta > 1$.

Finally we calculate the Poiseuille flow of an equimolar Ne–Ar mixture along channels of rectangular cross section, based on the hard-sphere model. To the best of our knowledge, the LBE for a gas mixture has not previously been solved in a two-dimensional geometry, because of the numerical complexity; we tackle the problem here by using the SIS and the fast spectral method [35]. The discretization of the spatial domain for a square cross section is the same as that in Sec. 2.4, while for a rectangular cross section of aspect ratio 2 the spatial domain is discretized by 50×100 cells, and the characteristic length ℓ is chosen to be the shorter side. Table 6 summarizes the LBE solution for the mass and heat flow rates in two-dimensional Poiseuille flow over a wide range of the rarefaction parameter. The iterations needed to achieve the convergence criterion $\epsilon = 10^{-7}$ are fewer than 40 when $\delta \leq 100$, demonstrating again the efficiency of the SIS. The normalized mass flow rates of Ne and Ar through the rectangular cross section with aspect ratio 2 are always larger than those in the aspect ratio 1 case. However, although the heat flow rates through the rectangular cross section with an aspect ratio of 2 are larger than those with the aspect ratio 1 when $\delta < 20$, they are roughly the same for $\delta \geq 20$. Typical velocity and heat flux profiles of the Ne–Ar gas mixture through the square cross section in the free molecular, transition, and near-continuum regimes are shown in Fig. 13, and are also compared to those of the single-species gas in the same geometry. From this figure we see that the velocity and heat flux of Ne is always larger than that of Ar, while the corresponding results for a single-species gas lie between those of Ne and Ar.

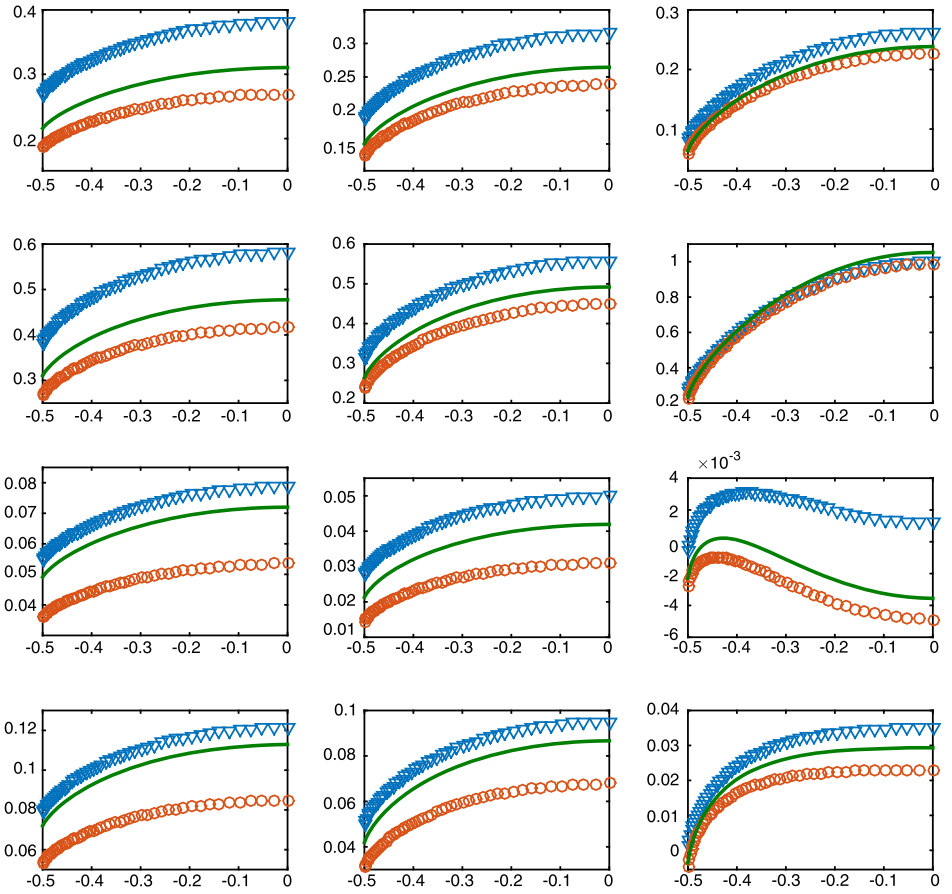

Fig. 13. Velocity ($\sqrt{m/m_A}U$) and heat flux ($\sqrt{m/m_A}q$) profiles in Poiseuille flow of an equimolar Ne–Ar gas mixture along a channel of square cross section, where $\delta = 0.1,\ 1,$ and 10 in the left, middle, and right columns, respectively. The first and second (third and fourth) rows show the velocity (heat flux) along the side and the center line of the cross section, respectively. Triangles: Ne, circles: Ar, while solid lines in the first and second (third and fourth) rows show the velocity (half heat flux) obtained from the single-species LBE.

6. Conclusions

We have proposed a synthetic iterative scheme to accelerate the convergence of the linearized Boltzmann equation for gas flows driven by pressure and temperature gradients in long channels. By penalizing the linearized Boltzmann collision operator L into the form $L = (L + NL_{BGK}) - NL_{BGK}$ or $L = (L + N\delta h) - N\delta h$, a diffusion-type equation has been derived for the macroscopic flow velocity. The velocity distribution function in the linearized Boltzmann equation was first solved by the conventional iterative scheme, where the linearized Boltzmann collision operator was approximated by the fast spectral method. Then the flow velocity was obtained by solving the diffusion-type equation, which was used to correct the velocity distribution function. In this way the slow convergence of the conventional iterative scheme in the near-continuum flow regime has been ameliorated: we found, through the numerical solution of Poiseuille and thermal transpiration flows, that the synthetic iterative scheme is faster than the conventional scheme by up to several orders of magnitude. More, it has been found that the synthetic iterative scheme is asymptotic-preserving into the Navier–Stokes level, so in the near-continuum regime the spatial resolution can be much larger than the molecular mean free path. This makes the synthetic iterative scheme much more faster and accurate than the conventional one, especially in multiscale problems with a wide variation of local flow length.

The tuning parameter N controls the convergence rate of the synthetic iterative scheme. In numerical investigations we found that for the linearized Boltzmann equation the fastest convergence is achieved when N roughly equals the ratio of the equilibrium collision frequency to the rarefaction parameter. Thus, N varies with the intermolecular potential: for a single-species gas, we found that the fastest convergence occurred with $N \approx 1.5$ for the hard-sphere gas model and $N \approx 2$ for the Maxwell gas model.

We also extended the synthetic iterative scheme to binary gas mixtures, and both the hard-sphere and Lennard–Jones intermolecular potentials have been considered. As an example, Poiseuille flow of a Ne–Ar mixture was simulated in order to test the computational performance as well as the influence of the intermolecular potential. The synthetic iterative scheme required only a limited number of iterations over the whole range of gas rarefaction. Based on this efficient scheme, the

Poiseuille flow of a Ne–Ar mixture between two parallel plates was simulated for the first time using the realistic Lennard–Jones potential. We found that the hard-sphere gas model overestimates the mass and heat flow rates when $\delta < 1$. Poiseuille flow of a Ne–Ar mixture through two-dimensional rectangular cross sections was also simulated using the linearized Boltzmann equation for the first time.

The developed method can also be extended to the efficient calculation of flows of multiple-species gas mixtures. In particular, our method can be applied to the McCormack model and we believe that the resulting diffusion-type equations for the flow velocity of each component will be much simpler than those in Refs. [18,23]. Our synthetic iterative scheme could also be applied straightforwardly to other canonical gas flows, such as Couette flow and the flow driven by a concentration gradient. However, it requires future work to investigate whether this method can be applied to other gas flow systems (such as the cavity flow) or not.

Acknowledgements

L. Wu acknowledges the financial support of an Early Career Researcher International Exchange Award from the Glasgow Research Partnership in Engineering. H. Liu gratefully acknowledges the financial support of the "Thousand Talents Program" for Distinguished Young Scholars, and the National Natural Science Foundation of China under Grant No. 51506168. This work is also financially supported in the UK by the Engineering and Physical Sciences Research Council (EPSRC) under grants EP/M021475/1, EP/L00030X/1, EP/K038621/1, and EP/N016602/1.

References

[1] C. Cercignani, Rarefied Gas Dynamics: From Basic Concepts to Actual Calculations, Cambridge University Press, Cambridge, New York, 2000.
[2] G.A. Bird, Molecular Gas Dynamics and the Direct Simulation of Gas Flows, Oxford Science Publications, Oxford University Press Inc, New York, 1994.
[3] L. Pareschi, G. Russo, Time relaxed Monte Carlo methods for the Boltzmann equation, SIAM J. Sci. Comput. 23 (2001) 1253–1273.
[4] B. Zhang, H. Liu, S. Jin, An asymptotic preserving Monte Carlo method for the multispecies Boltzmann equation, J. Comput. Phys. 305 (2016) 575–588.
[5] F.G. Tcheremissine, Direct numerical solution of the Boltzmann equation, AIP Conf. Proc. 762 (2005) 677–685.
[6] F. Filbet, S. Jin, A class of asymptotic-preserving schemes for kinetic equations and related problems with stiff sources, J. Comput. Phys. 229 (2010) 7625–7648.
[7] P.L. Bhatnagar, E.P. Gross, M. Krook, A model for collision processes in gases. I. Small amplitude processes in charged and neutral one-component systems, Phys. Rev. 94 (1954) 511–525.
[8] K. Xu, J.C. Huang, A unified gas-kinetic scheme for continuum and rarefied flows, J. Comput. Phys. 229 (2010) 7747–7764.
[9] E.M. Shakhov, Approximate kinetic equations in rarefied gas theory, Fluid Dyn. 3 (1968) 112–115.
[10] J.C. Huang, K. Xu, P.B. Yu, A unified gas-kinetic scheme for continuum and rarefied flows II: multi-dimensional cases, Commun. Comput. Phys. 12 (2012) 662–690.
[11] C. Liu, K. Xu, Q.H. Sun, Q.D. Cai, A unified gas-kinetic scheme for continuum and rarefied flow IV: full Boltzmann and model equations, J. Comput. Phys. 314 (2016) 305–340.
[12] S. Chen, K. Xu, A comparative study of an asymptotic preserving scheme and unified gas-kinetic scheme in continuum flow limit, J. Comput. Phys. 288 (2015) 52–65.
[13] Z. Guo, K. Xu, R.J. Wang, Discrete unified gas kinetic scheme for all Knudsen number flows: low-speed isothermal case, Phys. Rev. E 88 (2013) 033305.
[14] P. Wang, L.H. Zhu, Z. Guo, K. Xu, A comparative study of LBE and DUGKS methods for nearly incompressible flows, Commun. Comput. Phys. 17 (2015) 657–681.
[15] Y. Zhu, C. Zhong, K. Xu, Implicit unified gas-kinetic scheme for steady state solutions in all flow regimes, J. Comput. Phys. 315 (2016) 16–38.
[16] M.L. Adams, E.W. Larsen, Fast iterative methods for discrete-ordinates particle transport calculations, Prog. Nucl. Energy 40 (2002) 3–159.
[17] D. Valougeorgis, S. Naris, Acceleration schemes of the discrete velocity method: gaseous flows in rectangular microchannels, SIAM J. Sci. Comput. 25 (2003) 534–552.
[18] L. Szalmás, D. Valougeorgis, A fast iterative model for discrete velocity calculations on triangular grids, J. Comput. Phys. 229 (2010) 4315–4326.
[19] S. Naris, D. Valougeorgis, F. Sharipov, D. Kalempa, Discrete velocity modelling of gaseous mixture flows in MEMS, Superlattices Microstruct. 35 (2004) 629–643.
[20] S. Naris, D. Valougeorgis, D. Kalempa, F. Sharipov, Gaseous mixture flow between two parallel plates in the whole range of the gas rarefaction, Physica A 336 (2004) 294–318.
[21] S. Naris, D. Valougeorgis, D. Kalempa, F. Sharipov, Flow of gaseous mixtures through rectangular microchannels driven by pressure, temperature, and concentration gradients, Phys. Fluids 17 (2005) 100607.
[22] L. Szalmás, Accelerated discrete velocity method for axial-symmetric flows of gaseous mixtures as defined by the McCormack kinetic model, Comput. Phys. Commun. 184 (2013) 2430–2437.
[23] L. Szalmás, An accelerated discrete velocity method for flows of rarefied ternary gas mixtures in long rectangular channels, Comput. Fluids 128 (2016) 91–97.
[24] L. Szalmás, A fast iterative discrete velocity method for ternary gas mixtures flowing through long tubes, Comput. Phys. Commun. 200 (2016) 44–49.
[25] F. McCormack, Construction of linearized kinetic models for gaseous mixtures and molecular gases, Phys. Fluids 12 (1973) 2095–2105.
[26] T. Ohwada, Y. Sone, K. Aoki, Numerical analysis of the Poiseuille and thermal transpiration flows between two parallel plates on the basis of the Boltzmann equation for hard sphere molecules, Phys. Fluids 1 (1989) 2042–2049.
[27] T. Doi, Numerical analysis of the Poiseuille flow and thermal transpiration of a rarefied gas through a pipe with a rectangular cross section based on the linearized Boltzmann equation for a hard sphere molecular gas, J. Vac. Sci. Technol. A 28 (2010) 603–612.
[28] L. Wu, J.M. Reese, Y.H. Zhang, Solving the Boltzmann equation by the fast spectral method: application to microflows, J. Fluid Mech. 746 (2014) 53–84.
[29] F. Sharipov, G. Bertoldo, Poiseuille flow and thermal creep based on the Boltzmann equation with the Lennard–Jones potential over a wide range of the Knudsen number, Phys. Fluids 21 (2009) 067101.
[30] L. Wu, H.H. Liu, Y.H. Zhang, J.M. Reese, Influence of intermolecular potentials on rarefied gas flows: fast spectral solutions of the Boltzmann equation, Phys. Fluids 27 (2015) 082002.
[31] R.D.M. Garcia, C.E. Siewert, Channel flow of a binary mixture of rigid spheres described by the linearized Boltzmann equation and driven by temperature, pressure, and concentration gradients, SIAM J. Appl. Math. 67 (2007) 1041–1063.

[32] S. Jin, Q. Li, A BGK-penalization asymptotic-preserving scheme for the multispecies Boltzmann equation, Numer. Methods Partial Differ. Equ. 29 (2013) 1056–1080.
[33] G. Dimarco, L. Pareschi, Asymptotic preserving implicit-explicit Runge–Kutta methods for nonlinear kinetic equations, SIAM J. Numer. Anal. 51 (2013) 1064–1087.
[34] C. Mouhot, L. Pareschi, Fast algorithms for computing the Boltzmann collision operator, Math. Comput. 75 (2006) 1833–1852.
[35] L. Wu, J. Zhang, J.M. Reese, Y.H. Zhang, A fast spectral method for the Boltzmann equation for monatomic gas mixtures, J. Comput. Phys. 298 (2015) 602–621.
[36] J. Lihnaropoulos, S. Naris, D. Valougeorgis, Formulation and stability analysis of rapidly convergent iteration schemes for the 2-D linearized BGK equation, Transp. Theory Stat. Phys. 36 (2007) 513–528.
[37] L. Szalmás, An accelerated discrete velocity method for flows of rarefied ternary gas mixtures in long rectangular channels, Comput. Fluids 128 (2016) 91–97.
[38] F. Sharipov, Application of the Cercignani–Lampis scattering kernel to calculations of rarefied gas flows. II. slip and jump coefficients, Eur. J. Mech. B, Fluids 22 (2003) 133–143.
[39] E.M. Shakhov, Generalization of the Krook kinetic relaxation equation, Fluid Dyn. 3 (5) (1968) 95–96.
[40] F. Sharipov, Application of the Cercignani–Lampis scattering kernel to calculations of rarefied gas flows. III. Poiseuille flow and thermal creep through a long tube, Eur. J. Mech. B, Fluids 22 (2003) 145–154.
[41] M. Rojas-Cárdenas, I.A. Graur, P. Perrier, J.G. Méolans, Time-dependent experimental analysis of a thermal transpiration rarefied gas flow, Phys. Fluids 25 (2013) 072002.
[42] H. Yamaguchi, P. Perrier, M.T. Ho, J.G. Méolans, T. Niimi, I.A. Graur, Mass flow rate measurement of thermal creep flow from transitional to slip flow regime, J. Fluid Mech. 795 (2016) 690–707.
[43] P. Wang, M.T. Ho, L. Wu, Z. Guo, Y.H. Zhang, A comparative study of discrete velocity methods for rarefied gas flows, arXiv:1612.06590.
[44] M. Wang, J. Wang, N. Pan, S. Chen, Mesoscopic predictions of the effective thermal conductivity for microscale random porous media, Phys. Rev. E 75 (2007) 036702.
[45] L. Szalmás, D. Valougeorgis, Rarefied gas flow of binary mixtures through long channels with triangular and trapezoidal cross sections, Microfluid. Nanofluid. 9 (2010) 471–487.